Draft version November 4, 2025
Typeset using LaTeX **twocolumn** style in AASTeX7

Planets Across Space and Time (PAST). VIII: Kinematic Characterization and Identification of Radial Velocity Variables for the LAMOST-Gaia-TESS Stars

Di Wu [1,2] Di-Chang Chen [3,1,2] Ji-Wei Xie [1,2] Ji-Lin Zhou [1,2] Hai-Feng Wang [4] Weikai Zong [5,6]
Subo Dong [7,8,9] Maosheng Xiang [9] and A-Li Luo [9]

[1] School of Astronomy and Space Science, Nanjing University, Nanjing 210023, China
[2] Key Laboratory of Modern Astronomy and Astrophysics, Ministry of Education, Nanjing 210023, China
[3] School of Physics and Astronomy, Sun Yat-sen University, Zhuhai 519082, China
[4] Dipartimento di Fisica e Astronomia "Galileo Galilei", Universitá degli Studi di Padova, Vicolo Osservatorio 3, I-35122, Padova, Italy
[5] Institute for Frontiers in Astronomy and Astrophysics, Beijing Normal University, Beijing 102206, China
[6] School of Physics and Astronomy, Beijing Normal University, Beijing 100875, China
[7] Department of Astronomy, School of Physics, Peking University, 5 Yiheyuan Road, Haidian District, Beijing 100871, China
[8] Kavli Institute of Astronomy and Astrophysics, Peking University, 5 Yiheyuan Road, Haidian District, Beijing 100871, China
[9] National Astronomical Observatories, Chinese Academy of Science, 20A Datun Road, Chaoyang District, Beijing 100101, China

ABSTRACT

The Transiting Exoplanet Survey Satellite (TESS) has discovered over 6700 nearby exoplanets candidates using the transit method through its all-sky survey. Characterizing the kinematic properties and identifying variable stars for the TESS stellar sample is crucial for revealing the correlations between the properties of planetary systems and the properties of stars (e.g., Galactic components, age, chemistry, dynamics, radiation). Based on data from TESS, Gaia DR3, and LAMOST DR10, we present a catalog of kinematic properties (i.e., Galactic positions, velocities, orbits, Galactic components, and kinematic age) as well as other basic stellar parameters for $\sim 660,000$ TESS stars. Our analysis of the kinematic catalog reveals that stars belonging to different Galactic components (i.e., thin disk, thick disk, halo and 12 streams in the disk) display distinctive kinematic and chemical properties. We also find that hot planets with period less then 10 days in the TESS sample favor thin disk stars compared to thick disk stars, consistent with previous studies. Furthermore, using the LAMOST multiple-epoch observations, we identify 41,445 stars exhibiting significant radial velocity variations, among which 7,846 are classified as binary stars. By fitting the radial velocity curves, we further derive orbital parameters (e.g., mass ratio, orbital period and eccentricity) for 297 binaries. The catalogs constructed in this work have laid a solid foundation for future work on the formation and evolution of stellar and planetary systems in different Galactic environments.

Keywords: Catalogs (205) — Exoplanets (498) — Stellar ages (1581) — Binary stars (154) — Stellar Kinematics (1608)

1. INTRODUCTION

Since the first discovery of exoplanet orbiting Sun-like stars (Mayor & Queloz 1995), nearly 6,000 exoplanets have been discovered to date using various detection methods (e.g., radial velocity, direct imaging, astrometry, microlensing, and transit photometry) and thousands of candidates remain yet to be confirmed. Among these methods, the transit method has proven to be one of the most effective, accounting for the majority of known exoplanets (candidates) discoveries. Over the past two decades, several space-based transit surveys have been designed to search for large amounts of transiting exoplanets, from CoRoT (Baglin et al. 2006) and Kepler (Borucki et al. 2010; Borucki 2016), to the ongoing Transiting Exoplanet Survey Satellite (TESS) mission (Ricker et al. 2015).

In its first six years, TESS has identified approximately 7,000 planet candidates, with several hundred confirmed exoplanets (Stassun et al. 2018; Guerrero et al. 2021; Winn 2024). TESS has revealed numer-

Corresponding author: Di-Chang Chen; Ji-Wei Xie
chendch28@mail.sysu.edu.cn; jwxie@nju.edu.cn

ous intriguing targets orbiting bright and nearby stars that are particularly well-suited for follow-up observations. For example, it has contributed to the discovery of hundreds of super-Earths and mini-Neptunes (Huang et al. 2018; Günther et al. 2019), many of which have enabled precise mass measurements through radial velocity (RV) follow-up and detailed atmospheric characterization with the James Webb Space Telescope (JWST) (Lustig-Yaeger et al. 2023; Zhang et al. 2024). At the same time, TESS's all-sky coverage yields a large and diverse exoplanet sample, making it particularly valuable for statistical studies of planet populations. Ongoing efforts are exploring correlations between planetary properties and stellar characteristics, e.g., hot Jupiter occurrence across different stellar mass (Beleznay & Kunimoto 2022; Bryant et al. 2023), stellar types (Gan et al. 2023; Kanodia et al. 2024), and metallicities (Gan et al. 2025). Moreover, TESS has also significantly benefited the study in stellar physics, especially the identification and analyses of brown dwarfs (e.g., Carmichael 2023) and the variability of stars, including eclipsing binaries (Prša et al. 2022) , flaring stars (Feinstein et al. 2022; Xing et al. 2024), oscillating stars (Hon et al. 2021) and other types of variable stars (Plachy et al. 2021; Tu et al. 2021; Hasanzadeh et al. 2021).

However, the kinematics of TESS stars is yet to be well characterized and their impacts on the exoplanetary systems remain to be explored. Previous studies based on the Kepler field have already revealed several intriguing discoveries (e.g., Bashi & Zucker 2019; McTier & Kipping 2019; Bashi & Zucker 2022; Zink et al. 2023). For example, hot Jupiters are found to be preferentially hosted by kinematically younger stars, with their frequency declining significantly with stellar age, providing evidence for tidal decay and offering crucial insights into their origins and evolution (Hamer & Schlaufman 2019; Chen et al. 2023, Chen et al. 2025, submitted). Yang et al. (2023) demonstrated that Kepler planetary systems generally become dynamically hotter over time using the LAMOST-Gaia-Kepler kinematic catalogs (Chen et al. 2021a). However, Kepler's coverage is limited to a relative small region of the sky, raising the question of whether its findings can be generalized to the whole Milky Way. Moreover, plenty of Galactic substructures (e.g., associations, streams) have been identified in an all-sky region with distance $<$ 500 pc to our Sun (Cantat-Gaudin et al. 2018; Hasanzadeh et al. 2021; Bonaca & Price-Whelan 2025), offering a valuable opportunity to study the impacts of Galactic histories and stellar interactions on the planetary systems. With its all-sky survey of stars, TESS is well-suited to reveal the global picture of exoplanets across diverse Galactic environments and locations within the Milky Way.

To address these questions, the basis is to build a well-constructed kinematic catalog of TESS targets, containing their Galactic positions, velocities, orbits, component memberships, ages, and chemical abundances. The study conducted by Carrillo et al. (2020) constitutes a pioneering endeavor in this direction, which provided the spatial positions, Galactic velocities and Galactic membership for $\sim$ 2 million TESS stars by using astrometric and radial velocity data from Gaia DR2 and collected chemical properties (i.e., [Fe/H] and [α/Fe]) from several large spectroscopic surveys. However, their kinematic characterization was based on the methods of Bensby et al. (2003, 2014), which were primarily calibrated for stars within 100 pc and thus cannot be directly applied to TESS stars, which are distributed across a much broader range. Furthermore, their catalogs did not account for the identification of nearby substructures (e.g., stellar streams), which are suggested to have (potentially significant) impacts on planetary system properties (Winter et al. 2020; Dai et al. 2023). In addition, their use of heterogeneous spectroscopic datasets without cross-calibration introduces inconsistencies and selection biases toward planet-hosting stars (e.g., APOGEE).

In this work, to improve upon these limitations, we first adopt the revised kinematic methods from the PAST series (Chen et al. 2021a; Yang et al. 2023), which can be applied to stars within $\sim$2,000 pc for classification of Galactic components, thus covering most of TESS stars. The refined age-velocity dispersion relation (AVR) can also provide age estimations for groups of stars with a typical uncertainty of $\sim$10% - 20%. Secondly, we calculate the angular momentum and orbital actions to identify nearby stellar substructures following the methodology of Kushniruk & Bensby (2019). Moreover, to obtain a homogeneous catalog and ensure that the sample is unbiased toward planets, we rely on the spectroscopic data from LAMOST (the Large Sky Area Multi-Object Fiber Spectroscopic Telescope, also known as Goushoujing Telescope, Cui et al. 2012; Zhao et al. 2012), which provides stellar parameters, radial velocities, and elemental abundances (e.g., [Fe/H], [α/Fe]) uniformly derived from the LAMOST stellar parameter pipeline (Wu et al. 2014; Luo et al. 2015; Xiang et al. 2015). The LAMOST-TESS kinematic catalog enable statistic studies which can directly compare with those from LAMOST-Kepler kinematic data (e.g., Chen et al. 2022; Chen et al. 2023; Hamer & Schlaufman 2024), revealing the similarities and differences in the distribution and evolution of exoplanets in different positions of the Milky way.

Furthermore, this work leverages multiple epoch spectroscopy observations of the LAMOST medium-resolution (MRS) time-domain survey (Liu et al. 2020; Zong et al. 2020; Yan et al. 2022; Li et al. 2023), enabling the detection of variable and binary stars through RV variability. Using the systemic velocities derived from RV curve fitting, we can also characterize their kinematic properties. Numerous studies have used multi-epoch data for individual stars from wide-field spectroscopic surveys such as LAMOST, GALAH and APOGEE to search for and study RV variables and binaries (Gao et al. 2017; Badenes et al. 2018; Price-Whelan et al. 2018, 2020; Moe et al. 2019; Mazzola et al. 2020; Bashi et al. 2022; Guo et al. 2022). Variables and binary stars offer natural laboratories for testing fundamental astrophysics (Percy 2007). For instance, RR Lyrae variables are essential standard candles for cosmic distance measurements (Beaton et al. 2018) and also have been used to derive the structural parameters of the inner halo and thick disk (e.g., Mateu & Vivas 2018; Han et al. 2025). δ Scuti variables can provide insights into the scaling relations between astroseismology and stellar parameters (Hasanzadeh et al. 2021). On the other hand, interactions within binary systems can significantly influence stellar evolution (e.g., tidal decay, mergers; Raghavan et al. 2010; Sana et al. 2012; Duchêne & Kraus 2013; Moe & Di Stefano 2017; Chen et al. 2024). Moreover, the gravitational perturbations induced by binary companions can significantly affect planet formation and evolution (Holman & Wiegert 1999; Winn & Fabrycky 2015). For example, previous studies suggest that close stellar companions can influence protoplanetary disk dynamics and suppress planet formation, depending on the binary separation (Wang et al. 2014, 2015; Kraus et al. 2016; Ngo et al. 2016; Moe et al. 2019; El-Badry & Rix 2019). Binary-induced Kozai interactions can also affect the stability of planetary systems (Katz et al. 2011; Lithwick & Naoz 2011; Dong et al. 2014; Petrovich 2015a,b; Winn & Fabrycky 2015; Zhu & Dong 2021), and statistical studied have suggested that this mechanism can be crucial in the formation of hot Jupiters (Knutson et al. 2014; Ngo et al. 2015; Weldon et al. 2025). Therefore, the synergy combining TESS and LAMOST can provide a large dataset of variable and binary stars, together with the kinematic properties, it offers a valuable opportunity to explore stellar evolution and interaction, as well as their influence on planetary systems.

This work constitutes the eighth paper of the series of PAST (Planets Across Space and Time). Previously, we revised the kinematic method (PAST I, Chen et al. 2021a), constructed the LAMOST-Gaia-Kepler kinematic catalog (PAST II, Chen et al. 2021b), and applied the kinematic method and catalog to reveal the formation and evolution of various types of planets, e.g., Super Earth and Sub-Neptunes (PAST III-IV, Chen et al. 2022; Yang et al. 2023), Hot Jupiters (PAST V and VII, Chen et al. 2023, 2025) and Ultra Short Period (USP) planets (PAST VI, Tu et al. 2025). In this paper (PAST VIII), we kinematically characterize a large, homogeneous sample of TESS stars by using data from Gaia and LAMOST. Using multiple-epoch RV measurements from LAMOST, we identify RV variables and binary stars within the sample. For the binaries, we derive orbital parameters by fitting their RV curves, enabling reliable determination of their kinematic properties. The resulting binary catalog, which combines kinematic and orbital parameters, provides a solid foundation for investigating correlations between binary characteristics and stellar age, mass, and metallicity individually. Furthermore, the method of identifying RV variables can be applied to future LAMOST datasets or other large spectroscopic surveys to study how stellar multiplicity influences planetary systems. The catalogs presented in this work will thus facilitate future exploration of the formation and evolution of both planets and binary stars in the Galactic context.

This paper is organized as follows. In Section 2, we describe the construction of our sample from TESS, Gaia, and LAMOST. Section 3 outlines our methodology for kinematic characterization and stellar age estimation. In Section 4, we present the LAMOST-Gaia-TESS stellar catalog with kinematic and chemical properties. Section 5 demonstrates the process of identifying RV variables and binaries using the LAMOST MRS multiple-epoch catalog. Caveats and limitations are discussed in Section 6. Finally, we summarize our main findings in Section 7.

2. DATA COLLECTION

This section describes how we constructed the stellar sample from TESS (Section 2.1.1), Gaia (Section 2.1.2), and LAMOST (Section 2.1.3) for further kinematic characterization. In brief, we began with the TESS catalog and cross-matched it with Gaia to obtain astrometric data, i.e. positions, proper motions, and parallaxes. Radial velocities and other stellar spectral parameters were then incorporated from LAMOST spectroscopic data. To ensure data quality, we then applied filters to RV and spectroscopic data (Section 2.2). Based on these datasets, we can derive the space velocities and other kinematic properties for each star (with details discussed later in Section 3).

2.1. *Cross-match*

2.1.1. *TESS: Transiting Exoplanet Survey Satellite*

Our sample was initialized from the TESS Candidate Target List (CTL) v8.1, which is a curated subset of the TESS Input Catalog (TIC) v8.2 (Stassun et al. 2019; Paegert et al. 2021). The CTL consists of 9,488,282 targets selected as promising candidates for TESS transit detection, either with surface gravity values ($\log g$) indicative of dwarf stars or satisfying the criteria of TESS magnitudes $T \leq 13$ and stellar radii $\leq 5R_{\odot}$ (Stassun et al. 2019).

For the planetary sample, we incorporated data from the TESS Objects of Interest (TOI) catalog retrieved on November, 2024, which includes a total of 6,767 planet candidates after excluding false positives (FPs). Out of these candidates, 347 planets were first confirmed by TESS, while an additional 529 were classified as previously known planets.

2.1.2. *Astrometric Parameters from Gaia DR3*

We then cross-matched the CTL sample with Gaia DR3 to obtain astrometric data. Gaia DR3 provides sky positions (α, δ), parallaxes, and proper motions (μ_α, μ_δ) for more than 1.5 billion stars, spanning Gaia magnitudes from $G = 3$ to $G = 21$ (Lindegren et al. 2021; Gaia Collaboration et al. 2023a). Radial velocities (RVs) for ∼33.81 million stars were derived by combining the low-resolution BP/RP spectra with the medium-resolution RVS spectra (R ∼ 11,500) (Katz et al. 2023; Recio-Blanco et al. 2023). The uncertainties in RV depend on the brightness of the stars, increasing from ∼1.3 km s^{-1} at $G \approx 12$ to ∼6.4 km s^{-1} at $G \approx 14$. For a subset of 5.5 million bright stars, Gaia DR3 further provided astrophysical parameters including effective temperature ($T_{\rm eff}$), surface gravity ($\log g$), and metallicity ([M/H]), with median uncertainties of 120 K, 0.2 dex, and 0.14 dex, respectively. Additionally, the reliability of these parameters may be affected by systematic errors (Fouesneau et al. 2023; Gaia Collaboration et al. 2023a; Recio-Blanco et al. 2023), and previous studies indicate the accuracy of some derived parameters can be affected by input features such as extinction (A_G) (Zong et al. 2020).

The cross-match between the CTL sample and Gaia DR3 was performed using the X-match service provided by CDS (http://cdsxmatch.u-strasbg.fr). A separation limit of 1.5 arcseconds was adopted for the cross-matching. To ensure consistency in brightness, we applied a magnitude cut by inspecting the distribution of magnitude differences, setting the G magnitude difference to be less than 2. For cases where multiple matches satisfied these criteria for the same star, we kept the one with the smallest angular separation. Alternative methods were also tested, and yielded consistent results. We also removed potential binaries by eliminating stars with Gaia renormalized unit weight error (RUWE) > 1.2 following the recommendations of Lindegren et al. (2021) as binary orbits could affect the results of kinematic characterization. This criterion may also remove sources in crowded regions, intrinsically variable or bright stars, and active stars, whose astrometric solutions can deviate from the single-star model (Lindegren et al. 2021; Riello et al. 2021). The high-RUWE stars will be included in Section 5.1, where we provide a detailed analysis of binaries in our sample.

2.1.3. *RV and Stellar Properties from LAMOST*

We supplemented our catalog with spectra data from LAMOST DR10, which provides RVs, metallicity, and other stellar parameter measurements. LAMOST DR10 includes both low- and medium-resolution spectroscopic surveys (hereinafter LRS and MRS respectively). The LRS observational mode has a resolution of R ∼ 1800 and covers wavelengths from 3700 − 9000Å, providing over 11.4 million spectra. Stellar parameters derived from LRS are available for over 7.4 million A, F, G, and K-type stars, uncertainties of 120 K for $T_{\rm eff}$, 0.2 dex for $\log g$, 0.1 dex for [Fe/H] and ∼ 3 - 5 km s^{-1} for RV, depending on the signal-to-noise ratio (SNR) (Luo et al. 2015).

The MRS mode offers higher precision with R ∼ 7500 and two wavelength ranges: 4950 − 5350Å and 6300 − 6800Å, covering 2,148,470 stars. Compared to LRS, MRS improves parameter accuracy, with typical uncertainties for $T_{\rm eff}$, $\log g$, [Fe/H] and RV reduced to ∼100 K, ∼0.1 dex, 0.06 − 0.12 dex and ∼1 km s^{-1}, respectively (Liu et al. 2020). Moreover, the higher resolution of MRS provided measurements of detailed chemical abundances for 12 individual elements, including C, N, O, Mg, and Ti (Yan et al. 2022).

To evaluate the reliability of the LAMOST MRS and Gaia RVS data, we compared RV, $T_{\rm eff}$, $\log g$, and [Fe/H] measurements from both LAMOST and Gaia with APOGEE as a benchmark. As shown in Figure 1, both LAMOST and Gaia RVS show good agreement with APOGEE for RV, exhibiting a linear correlation with the slope close to unity. However, in the case of other parameters, LAMOST demonstrates better consistency, while Gaia exhibits more significant deviations. For $T_{\rm eff}$, LAMOST has a slope of 0.63, with deviations of ∼250 K for $T_{\rm eff}$ ranging from 6000K to 6500 K. In

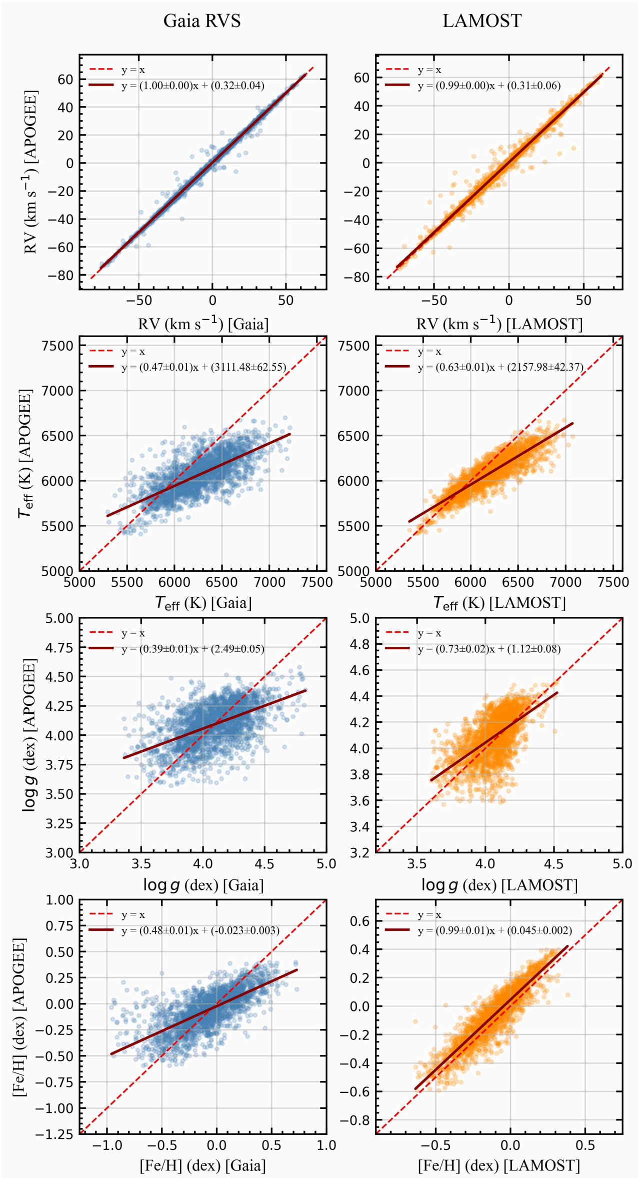

Figure 1. Radial velocity and stellar parameters obtained from Gaia RVS (left panel) and LAMOST (right panel) in comparison with APOGEE. Dark red fitted regression lines illustrate the correlations between the respective datasets, with slope and intercept values indicated. The line $y = x$ is plotted as a red dashed line for reference.

contrast, Gaia's $T_{\rm eff}$ scale has a shallower slope (0.47). For stars with $T_{\rm eff} > 6000$ K, Gaia can underestimate temperatures by > 500 K compared to APOGEE. In the case of $\log g$, LAMOST maintains a slope of 0.73, while Gaia shows a slope of 0.39, resulting in underestimates of $\sim$0.5 dex at $\log g = 4.2$. The difference is most prominent for [Fe/H], where LAMOST measurements are nearly identical to APOGEE (slope of 0.99 ± 0.01), whereas Gaia shows a significant deviation (slope of 0.48 ± 0.01), suggesting systematic errors in Gaia's measurements. Given the consistency of LAMOST MRS with APOGEE and the systematic biases in Gaia's spectroscopic parameters, we adopt LAMOST MRS measurements for characterizing the kinematic and chemical properties of the CTL-Gaia sample.

The CTL-Gaia sample was cross-matched with both the LAMOST DR10 LRS and MRS stellar parameter catalogs using the same procedure described in Section 2.1.2, with a separation limit of 1.5 arcseconds. Additionally, we applied a quality cut of SNR > 10. After the cross-matching and selections, we constructed two samples consisting of astrometric data from Gaia, along with RVs, atmospheric parameters, and chemical compositions from LAMOST. The MRS sample included 386,867 stars and 357 planets, while the LRS sample included 950,503 stars and 656 planets.

2.2. *Data Reduction*

To ensure data quality, we further applied the following filters:

1. Consistency Check Between LRS and MRS: Stars with significant differences in $T_{\rm eff}$, RV, [Fe/H], and [α/Fe] measurements between DR10 LRS and MRS were removed. To address systematic differences and offsets in the measurements between the DR10 LRS and MRS, we performed a fitting analysis. First, outliers beyond a 3σ threshold were removed from the common sample. A linear relation of the form $X_{\rm LRS} = k \cdot X_{\rm MRS} + b$ was then fitted using least-squares regression, where X represents the measured parameters. Residuals were calculated as $\Delta X = X_{\rm LRS} - k \cdot X_{\rm MRS} - b$ and measurements with residuals exceeding twice their typical uncertainties ($|\Delta X| > 2\sigma$) were considered as inconsistent and excluded from the sample.

2. Comparison Between LAMOST DR10 and DR9: Following the similar procedure, stars with significant differences in $T_{\rm eff}$, RV, [Fe/H], and [α/Fe] measurements between DR10 and DR9 were removed.

3. Comparison with TESS and Gaia: Stars with significant differences in $T_{\rm eff}$ measurements between TESS, Gaia, and LAMOST were removed with similar procedure as before.

After completing the above cross-match and data reduction process, we only kept stars with a distance less than 2 kpc to the sun, which is the applicable limit of the revised kinematic characteristics and age-velocity relation (AVR) in PAST series (Chen et al. 2021a; Yang et al. 2023). The final MRS sample consists of 207,690 stars and 223 planet candidates. We found that 117,632 stars in the LRS sample also have corresponding MRS spectra, as they were observed by both programs. To ensure the LRS and MRS samples are mutually exclusive, for the LRS sample, we retained only those stars without MRS coverage, resulting in a final LRS sample of 452,803 stars and 321 planet candidates. The composition of the sample after each processing step is summarized in Table 1.

Additionally, LAMOST MRS time-domain survey provided repeated observations and RV measurements for 547,726 stars in the LAMOST DR10 MRS dataset. These multiple-epoch observations are utilized in Section 5 to construct a catalog of RV variable stars for subsequent binary analysis, without applying RUWE or RV consistency filters.

Table 1. Construction of the LAMOST-Gaia-TESS star sample

(a) LRS

Selection Criteria	$N_{\rm s}$	$N_{\rm p}$
CTL	9,488,272	6,767
Crossmatch with LAMOST_LRS DR10	970,373	659
SNR > 10	950,503	656
Crossmatch with Gaia DR3	927,801	629
No binary	666,717	470
Reliability with LAMOST DR9	638,673	457
Reliability with LAMOST_MRS DR10	620,292	438
$T_{\rm eff}$ reliability	571,530	413
Distance < 2 kpc	570,435	413
Without MRS spectra	452,803	321

(b) MRS

Selection Criteria	$N_{\rm s}$	$N_{\rm p}$
CTL	9,488,272	6,767
Crossmatch with LAMOST_MRS DR10	388,110	659
SNR > 10	386,867	357
Crossmatch with Gaia DR3	381,290	349
No binary	270,973	270
Reliability with LAMOST DR9	235,986	251
Reliability with LAMOST_LRS DR10	222,132	232
$T_{\rm eff}$ reliability	207,776	223
Distance < 2 kpc	207,690	223

NOTE—$N_{\rm s}$ and $N_{\rm p}$ are the numbers of stars and planets (TOIs), respectively, during the process of sample selection in Section 2.2. $T_{\rm eff}$ reliability includes both comparison with Gaia and TESS.

3. METHODS FOR CLASSIFICATION OF GALACTIC COMPONENTS AND ESTIMATION OF AGES

In this Section, we describe how we calculate the stellar kinematics (i.e., space position and Galactic orbits; Section 3.1), classify star into different Galactic components (Section 3.2) and estimate stellar ages (Section 3.3).

3.1. *Space Position and Galactic Orbits*

We determined the 3D Galactocentric cylindrical coordinates (R, θ, Z) using the Solar position of $R_{\odot}=$ 8.18 kpc and $Z_{\odot} = 27$ pc (The GRAVITY Collaboration et al. 2019; Gaia Collaboration et al. 2023a). Galactic velocities (U, V, W) in the Cartesian Galactic system were calculated from the LAMOST RV and Gaia astrometric data, following the equations in Johnson & Soderblom (1987). We adopt a right-handed Galactic coordinate system, where U points toward the Galactic center, V follows the direction of rotation, and W is directed toward the North Galactic Pole (NGP). To derive the Galactic rectangular velocities with respect to the local standard of rest (LSR), we adopt the Solar peculiar motion $[U, V, W]$ = [9.58, 10.52, 7.01] km s^{-1}, as reported by Tian et al. (2015). Uncertainties in the velocity components U, V, and W were propagated from measurement errors in distances, proper motions, and RVs using the method introduced by Johnson & Soderblom (1987). The cylindrical velocities V_R, V_θ, and V_Z are considered positive with the increases in R, θ, and Z respectively, with V_Z increasing towards the North Galactic Pole. Furthermore, we calculate the orbital angular momentum(L_X, L_Y, L_Z) and orbital actions (J_R, J_Z) using an axisymmetric potential model of the Milky Way implemented in the Python package *gala* (Price-Whelan 2017) with the potential model including a spherical galactic nucleus and bulge, a three-component sum of Miyamoto–Nagai galactic disks and a spherical Navarro–Frenk–White dark matter halo model (Navarro et al. 1996). The galactic rotation curve and the vertical structure of the Galactic disks are set by the velocity curve from Eilers et al. (2019) and the shape of the phase-space spiral from Darragh-Ford et al. (2023), respectively.

3.2. *Classification of Galactic Components*

We first identified stars belonging to stellar streams (e.g., Arcturus, Sirius, and Pleiades/Pleiades/Hyades) by adopting the velocity, angular momentum, and action planes in Kushniruk & Bensby (2019). For the remaining stars, with the refined kinematic method (Section 2.2 of Chen et al. 2021b) and updated typical characteristics based on Gaia DR3 data (Table 2 of Yang et al. 2023), we calculate the probabilities of stars belonging to each Galactic component, i.e., thin disk (D), thick disk (TD), halo (H), and the Hercules stream (Herc). Stars were then classified into these Galactic components following the same criteria in Bensby et al. (2014).

3.3. *Kinematic Age*

3.3.1. *Average Kinematic Age from Velocity Dispersion*

As described in Section 3.6 of PAST I (Chen et al. 2021b), for a group of stars, the average kinematic age can be derived using the age-velocity dispersion relation (AVR), expressed as:

$$\mathrm{Age_{kin}} = \left(\frac{\sigma}{k\,\mathrm{km\ s^{-1}}}\right)^{\frac{1}{\beta}}\ \mathrm{Gyr}, \quad (1)$$

where σ is the velocity dispersion, which is defined as the root mean square of stellar Galactic velocity. The parameters k, β are the fitting coefficients of AVR, adopted from Table 4 of Yang et al. (2023) based on Gaia DR3 and LAMOST MSTO-SG catalog. The uncertainty of Age_{kin} is propagated from the errors in k, β and σ, yielding a typical uncertainty of $\sim 10\% - 20\%$.

3.3.2. *Individual Age from J_Z*

Sagear et al. (2024) proposed a flexible model and a software package *zoomies*[10] to predict stellar ages $\mathrm{Age_{zoomies}}$ for individual stars based on their vertical action J_Z. We also used the *zoomies* package to estimate ages for our LAMOST-Gaia-TESS sample. Nevertheless, the typical uncertainties in the derived $\mathrm{Age_{zoomies}}$ are quite large as $\sim 3 - 4$ Gyr (see Figure. 15 of Sagear et al. 2024), limiting their applicability to providing only a rough estimate of the age range.

4. THE CATALOG OF LAMOST-GAIA-TESS STARS WITH KINEMATIC CHARACTERISTICS

Applying the methods described in Section 3 to the LAMOST-Gaia-TESS sample, we characterize the kinematic properties including space position, Galactic orbits, the relative membership probabilities between different Galactic components (TD/D, TD/H, $Herc/D$ and $Herc/TD$), and kinematic age for 207,690 and 452,803 TESS stars with LAMOST MRS and LRS spectral data, respectively (Table 2). For clarity and conciseness, we present results primarily for the MRS sample in this section, while those for the LRS sample are provided in Figures A1–A6 in the Appendix. Figure 2 presents the spatial distribution of stars in the MRS sample. As can be seen, the majority of stars are located within the region $|Z| < 1.0$ kpc and $7.5 < R < 9.5$ kpc.

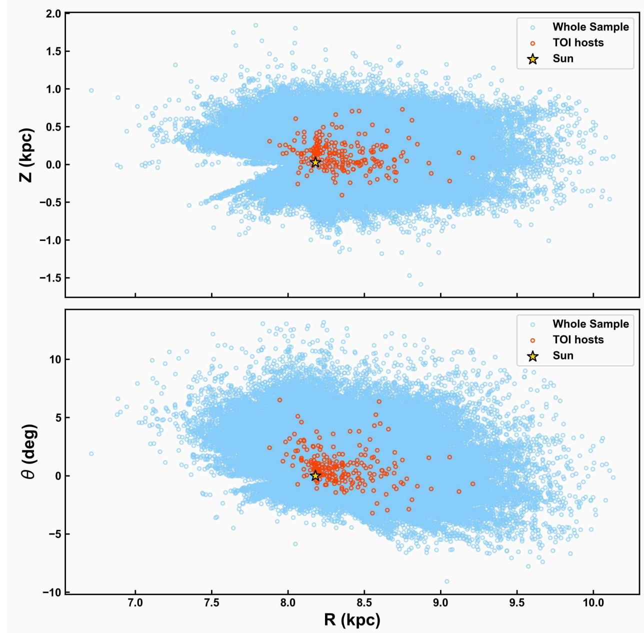

Figure 2. Top panel: Galactocentric radius (R) vs. height (Z) for the LAMOST_MRS-Gaia-TESS sample. A yellow star marks the location of the Sun (8.18 kpc, 0.027 kpc). Bottom panel: Galactocentric radius (R) vs. angle (θ) for the MRS sample, with (8.18 kpc, 0°) marking the position of Sun. Red points represent the TOI host stars.

[10] www.github.com/ssagear/zoomies

Table 2. The catalog of the LAMOST_MRS-Gaia-TESS star sample

Column	Name	Format	Units	Description
				Parameters obtained from Gaia, LAMOST and TESS
1	Gaia DR3 ID	Long		Unique Gaia source identifier
2	LAMOST ID	String		LAMOST unique spectral ID
3	TIC	Integer		TESS Input Catalog (TIC) ID
4	Gaia RA	Double	deg	Barycentric right ascension
5	Gaia Dec	Double	deg	Barycentric Declination
6	Gaia parallax	Double	mas	Absolute stellar parallax
7	Gaia e_parallax	Double	mas	Standard error of parallax
8	Gaia pmra	Double	mas yr^{-1}	Proper motion in right ascension direction
9	Gaia e_pmra	Double	mas yr^{-1}	Standard error of proper motion in right ascension direction
10	Gaia pmdec	Double	mas yr^{-1}	Proper motion in declination direction
11	Gaia e_pmdec	Double	mas yr^{-1}	Standard error of proper motion in declination direction
12	Gaia G mag	Double		Gaia G band apparent magnitude
13	TESS mag	Double		TESS apparent magnitude
14	Radius	Double	$R_\odot$	Stellar radius from TESS
15	e_radius	Double	$R_\odot$	Uncertainty of stellar radius
16	Mass	Double	$M_\odot$	Stellar mass from TESS
17	e_mass	Double	$M_\odot$	Uncertainty of stellar mass
18	$T_{\rm eff}$	Float	K	Effective temperature from LAMOST
19	$e\_T_{\rm eff}$	Float	K	Error of effective temperature
20	$\log g$	Float		Surface gravity from LAMOST
21	$e\_\log g$	Float		Error of surface gravity
22	[Fe/H]	Float	dex	Metallicity from LAMOST
23	e_[Fe/H]	Float	dex	Error of Fe element abundance
24	[α/Fe]	Float	dex	Alpha abundance from LAMOST
25	e_[α/Fe]	Float	dex	Error of alpha elements abundance
26	[C/Fe]	Float	dex	Element abundance of C from LAMOST
27	[N/Fe]	Float	dex	Element abundance of N from LAMOST
28	[O/Fe]	Float	dex	Element abundance of O from LAMOST
29	[Mg/Fe]	Float	dex	Element abundance of Mg from LAMOST
30	[Al/Fe]	Float	dex	Element abundance of Al from LAMOST
31	[Si/Fe]	Float	dex	Element abundance of Si from LAMOST
32	[S/Fe]	Float	dex	Element abundance of S from LAMOST
33	[Ca/Fe]	Float	dex	Element abundance of Ca from LAMOST
34	[Ti/Fe]	Float	dex	Element abundance of Ti from LAMOST
35	[Cr/Fe]	Float	dex	Element abundance of Cr from LAMOST
36	[Ni/Fe]	Float	dex	Element abundance of Ni from LAMOST
37	[Cu/Fe]	Float	dex	Element abundance of Cu from LAMOST
38	RV source flag	Float		RV source described in Section 6
39	$v_{\rm r}$	Double	km s^{-1}	Radial velocity from LAMOST
40	$e\_v_{\rm r}$	Double	km s^{-1}	Error of radial velocity

Table 2 *continued*

Table 2 *(continued)*

Column	Name	Format	Units	Description
41	TOI Flag	Boolean		True if the star hosts TOI
42	$N_{\rm p}$	Integer		Planet (candidate) multiplicity
43	Full TOI ID	String		Unique TESS Object of Interest identifier
44	TESS Disposition	String		Planet disposition from TESS
45	$M_{\rm p}$	String	$M_{\oplus}$	Planet mass
46	Period	String	days	Planet orbital period
47	e_period	String	days	Error of orbital period
48	$R_{\rm p}$	Double	$R_{\oplus}$	Planet radius
49	$e\_R_{\rm p}$	Double	$R_{\oplus}$	Error of planet radius
50	Temp	Double	K	Planet equilibrium temperature
				Parameters derived
51	R	Double	kpc	Galactocentric Cylindrical radial distance
52	θ	Double	deg	Galactocentric Cylindrical azimuth angle
53	Z	Double	kpc	Galactocentric Cylindrical vertical height
54	$U_{\rm LSR}$	Double	km s^{-1}	Cartesian Galactocentric x-velocity to the LSR
55	$e\_U_{\rm LSR}$	Double	km s^{-1}	Error of Cartesian Galactocentric x-velocity to the LSR
56	$V_{\rm LSR}$	Double	km s^{-1}	Cartesian Galactocentric y-velocity to the LSR
57	$e\_V_{\rm LSR}$	Double	km s^{-1}	Error of Cartesian Galactocentric y-velocity to the LSR
58	$W_{\rm LSR}$	Double	km s^{-1}	Cartesian Galactocentric z-velocity to the LSR
59	$e\_W_{\rm LSR}$	Double	km s^{-1}	Error of Cartesian Galactocentric z-velocity to the LSR
60	L_X	Double	kpc km s^{-1}	Galactocentric x-angular momentum
61	L_Y	Double	kpc km s^{-1}	Galactocentric y-angular momentum
62	L_Z	Double	kpc km s^{-1}	Galactocentric z-angular momentum
63	J_R	Double	kpc km s^{-1}	Radial orbital action
64	J_Z	Double	kpc km s^{-1}	Vertical orbital action
65	t_{J_Z}	Double	Gyr	kinematic age derived from J_Z using *zoomies*
66	$t_{J_Z}^{Up}$	Double	Gyr	1-σ upper limit of kinematic age derived from J_Z using *zoomies*
67	$t_{J_Z}^{Lower}$	Double	Gyr	1-σ lower limit of kinematic age derived from J_Z using *zoomies*
68	TD/D	Double		Thick disc to thin disc membership probability
69	TD/H	Double		Thick disc to halo membership probability
70	$Herc/D$	Double		Hercules stream to thin disc membership probability
71	$Herc/TD$	Double		Hercules stream to thick disc membership probability
72	Component	String		Classification of Galactic components

Note—Table 2 is published in its entirety in the machine-readable format. A column description is shown here for guidance regarding its form and content.

Based on their velocity, angular momentum, and action, we identify stars associated with nearby stellar streams by adopting the $U-V$, $V-\sqrt{U^2+2V^2}$, $L_Z-\sqrt{L_X^2+L_Y^2}$ and L_Z-J_R planes characteristics according to Kushniruk & Bensby (2019). The remaining stars are then classified into four Galactic components, i.e., thin disk, thick disk, Hercules stream and halo based on the calculated relative membership probabilities between different Galactic components, following the previously mentioned criteria. For stars not assigned to any of these components, we place them in a category termed "in between," following the classification in Bensby et al. (2014).

Table 3 summarizes the number of stars and planets, as well as the kinematic properties and chemical abun-

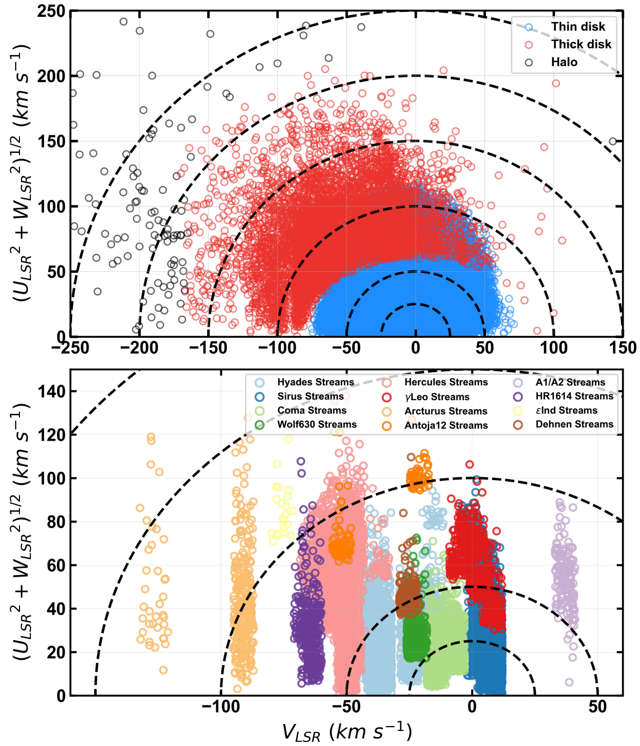

Figure 3. The Toomre diagram of LAMOST_MRS-Gaia-TESS stars for different Galactic components (top panel) and stellar streams (bottom panel). Different color represents different memberships. Dotted lines indicate constant values of the total Galactic velocity V_{tot} in stpdf of 25 km s^{-1} and 50 km s^{-1}.

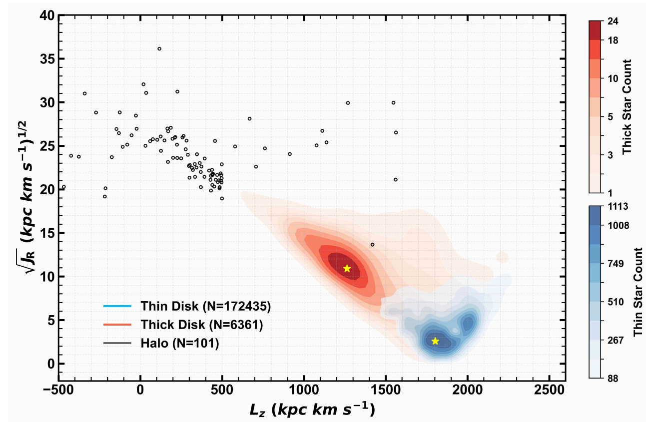

Figure 4. The distribution of disk stars in the vertical angular momentum L_z vs. radial action $\sqrt{J_{\rm R}}$ plane for the LAMOST_MRS-Gaia-TESS sample, with the thin disk ($N = 172,435$), thick disk ($N = 6,361$) and halo ($N = 101$) populations shown in blue, red, and black, respectively. Contour density maps illustrate the stellar distributions, with darker regions indicating higher star densities, the peak density location for each component is marked with a yellow star. Colorbars for each component are scaled separately since their sample sizes differ significantly, the ticks show an estimated number of sample in each grid. As shown, different components occupy distinct regions in the L_z-J_R plane, reflecting their kinematic differences.

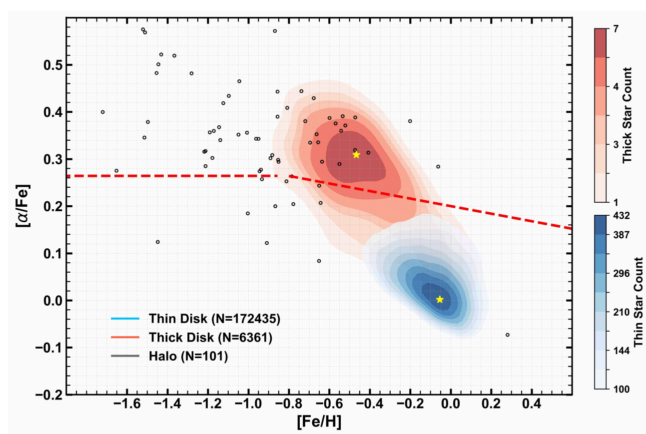

Figure 5. Same as Figure 4 but for the distribution in the [α/Fe] vs. [Fe/H] plane for the LAMOST_MRS-Gaia-TESS sample. The red dashed line represents the division between the thick and thin disks from Lee et al. (2011), the distribution reveals distinct chemical abundance trends among these populations.

dances of different Galactic components for the MRS samples (See Table A1 in the Appendix A for the LRS sample). As can be seen, for the MRS sample, approximately 83.0% (172,435/207,690) of the stars belong to the thin disk, while approximately 3.1% (6,361/207,690) are in the thick disk. The fraction of stars belonging to the halo is about 0.05% (101/207,690). Additionally, $\sim$ 8.0% (16,551/207,690) of the stars are classified into 12 distinct stellar streams.

To illustrate the kinematic properties, we plot the Toomre diagram and the vertical angular momentum (L_Z)-radial action ($\sqrt{J_{\rm R}}$) distributions of the LAMOST_MRS-Gaia-TESS stars in Figure 3 and Figure 4, respectively. As shown, most stars in the thin disk have low velocities $\left(V_{\rm tot} \lesssim 70 \text{ km s}^{-1}\right)$, high vertical angular momentum ($L_Z \sim 1500 - 2500$ kpc km s^{-1}) and low radial action ($\sqrt{J_{\rm R}} \lesssim 5$ kpc$^{1/2}$ km$^{1/2}$ s$^{-1/2}$) while thick disk stars mainly exhibit moderate velocities $\left(V_{\rm tot} \sim 70 - 180 \text{ km s}^{-1}\right)$, vertical angular momentum in the range $L_Z \sim 900 - 2000$ kpc km s^{-1} and elevated radial action ($\sqrt{J_{\rm R}} \sim 5 - 20$ kpc$^{1/2}$ km$^{1/2}$ s$^{-1/2}$). Halo stars typically have velocities exceeding 200 km s^{-1}, along with the lowest vertical angular momentum of $L_Z \lesssim 500$ kpc km s^{-1} and highest radial action of $\sqrt{J_{\rm R}} > 20$ kpc$^{1/2}$ km$^{1/2}$ s$^{-1/2}$.

The distribution of chemical abundances of the disk stars is presented in Figure 5, along with their number density. As shown, thick disk stars are more metal-poor

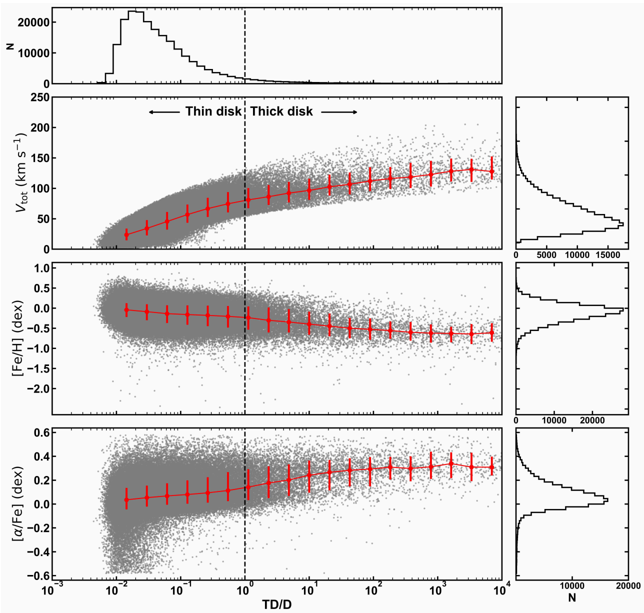

Figure 6. Kinematic and chemical properties (from top to bottom: total velocity $V_{\rm tot}$, [Fe/H] and [α/Fe]) as functions of the relative probability between thick disk to thin disk (TD/D) for the LAMOST_MRS-Gaia-TESS stars. The vertical dashed lines indicate where TD/D = 1. Medians and 1σ dispersion for different TD/D groups are marked in the plots. Histograms of TD/D and kinematic/chemical properties are displayed in the topmost and right panels, respectively.

([Fe/H] ~ -0.45) and alpha-enhanced ([α/Fe] ~ 0.26) compared to thin disk stars. These two populations are clearly distinguishable in the [Fe/H]-[α/Fe] plane, as previously suggested by Lee et al. (2011) using a G-dwarf sample from SEGUE. For halo stars, as expected, they exhibit the highest [α/Fe] values, reaching up to ~ 0.4 dex (see Table 3). Their metallicities span a wide range, from [Fe/H] of –2 dex to –0.2 dex, and the population can be broadly divided into metal-poor ([Fe/H]<–1) and metal-rich ([Fe/H]>–1) subgroups, which is consistent with previous studies that combined Gaia data with Apogee, RAVE, and LAMOST surveys (Bonaca et al. 2017; Posti et al. 2018; Fernández-Alvar et al. 2019; Belokurov et al. 2020; Yan et al. 2020; Zhu et al. 2021). As discussed in earlier studies, metal-rich halo stars may have formed in-situ within the Galactic disk and were later dynamically heated during merger events, altering their orbits to exhibit halo-like motion. In contrast, the canonical metal-poor halo stars are generally believed to have been largely accreted from satellite galaxies (Conroy & Wechsler 2009; Yan et al. 2020). In Figure 6, we plot the total velocity $V_{\rm tot}$, [Fe/H], and [α/Fe] as a function of TD/D. As shown, with the increasing of TD/D, $V_{\rm tot}$ and [α/Fe] increase, while [Fe/H] decreases.

Moreover, Figure 7 displays the [Fe/H] $-$ [α/Fe] distributions of stars in the 12 streams, color-coded by their $V_{\rm tot}$. Stars in a given stream exhibit similar total velocities ($V_{\rm tot}$), vertical angular momenta (L_Z), and radial orbital actions (J_R) (see Table 3), suggesting that they share a common origin. As seen in Figure 7 and Table 3, from the chemo-kinematics, we find that the Coma stream is metal-richer and alpha-poorer, with lower velocities ($V_{\rm tot}$) and orbital actions (J_R, J_Z) compared to the thin disk. The chemical and kinematic properties of the Sirius and Wolf630 streams are similar to those of the thin disk. For the Hercules, Pleiades/Hyades, Dehnen, and HR 1614 streams, their velocities, vertical angular momentums (L_Z), orbital actions and chemical abundances all lie between those of the thin and thick disks, which is consistent with previous studies (e.g., Bensby et al. 2014; Kushniruk et al. 2020) and indicates that they are likely mixtures of the thin and thick disks. The Arcturus and ϵInd streams in our sample have $V_{\rm tot} \sim 100$ km s^{-1}, low angular momentum, and high orbital actions, with chemical compositions similar to the thick disk. We also notice that stars in the A1/A2 and γ Leo streams have the highest L_Z (similar to very thin disk stars), but their other properties do not match those of thin disk stars.

For the planetary sample, there are 544 TESS planet candidates in the LAMOST-Gaia-TESS catalog, with 321 in the LRS and 223 in the MRS. As shown in Figure 2, most planet candidates in our sample are located within the region of $R \sim 8.0 - 8.5$ kpc and $|Z| < 0.5$ kpc. Figure 8 illustrates the period-radius distributions of these planet candidates from both the LRS and MRS samples across different Galactic components. As can be seen, the majority (84.7%, 461/544) of TESS planet candidates are hosted by thin disk stars. Additionally, 0.9% (5/544) and 9.6%(52/544) of TESS planet candidates are found orbiting stars in the thick disk and stellar streams, respectively, while no planets are detected around halo stars. Without considering observational biases, the number ratio of planets over stars in the thin disk (0.27%, 461/172,435) appears to be higher by a factor of three than that in the thick disk (0.08%, 5/6,361). Most planets in the thin disk exhibit short orbital periods ($P < 10$ days), with the majority being hot Jupiters, which is consistent with observational selection efficiency. In contrast, for the thick disk stars, 5 warm planets are found, but no hot Jupiters are detected. This indicates that hot Jupiters are unlikely to form or survive around thick disk stars, which is consistent with previous studies (Chen et al. 2023): Thick disk stars are metal-poor with a low frequency of hot Jupiters (Johnson et al. 2010; Guo et al. 2017) and are

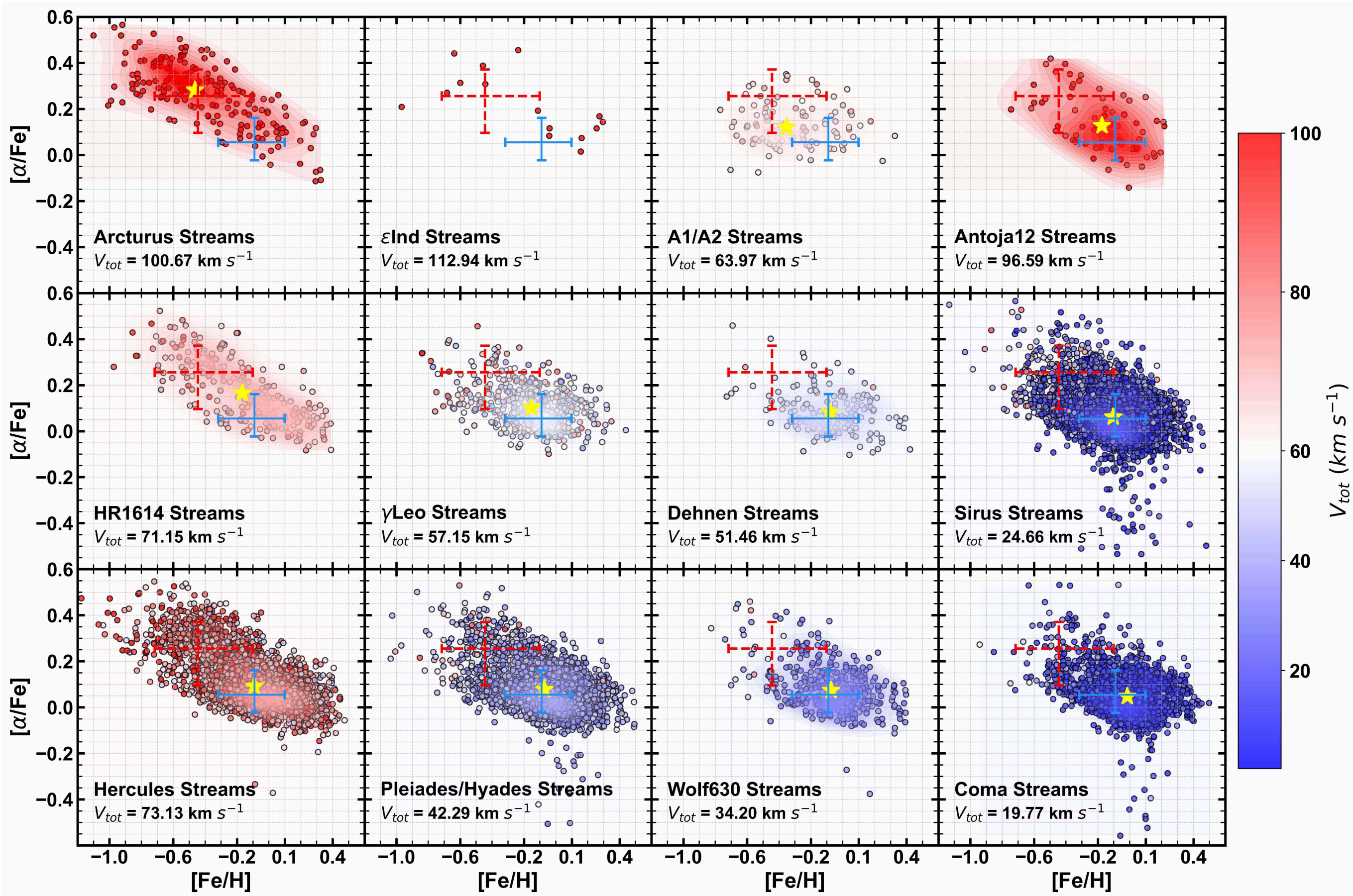

Figure 7. Distribution and number density of stellar streams in the [Fe/H] vs. [α/Fe] plane for LAMOST_MRS-Gaia-TESS sample. Each subplot represents a unique stellar stream, with data points color-coded by $V_{\rm tot}$ and arranged from top-left to bottom-right according to [Fe/H]. Contour lines indicate stellar density, where darker shades represent higher densities, while a yellow star denotes the typical value of [Fe/H] for each stream. The two error bars represent the values for thin disk stars (blue solid line) and thick disk stars (red dashed line) for reference.

old enough that some hot Jupiters may have undergone tidal orbital decay and disruption (Jackson et al. 2009; Levrard et al. 2009).

5. CATALOGS OF RV VARIABLES FROM LAMOST MULTIPLE EPOCH OBSERVATION

Binary systems and variable stars can be identified using various methods. For example, by analyzing light curves, previous studies have identified eclipsing binaries by analyzing light curves based on Kepler and TESS data (Prša et al. 2011, 2022). Through astrometric measurements, Gaia provides numerous wide binaries (El-Badry et al. 2021). In some cases, binary systems can also be detected directly from spectral features, such as double-lined spectroscopic binaries (SB2s), which exhibit two distinct sets of spectral lines (El-Badry et al. 2018; Traven et al. 2020). On the other hand, analyzing time-domain RV data from spectroscopic surveys are particularly effective in identifying close binaries (Price-Whelan et al. 2018, 2020; Chen et al. 2024), especially for the systems remain unresolved in photometric or spectroscopic observations.

In this Section, we search for RV variables within the LAMOST-Gaia-TESS catalog. Utilizing the time-domain RV data from the LAMOST MRS multiple epoch observations, we identify RV variable stars and binary stars, as presented in Table 4. For a subset of binary candidates, we further derive orbital parameters by fitting their radial velocity curves (see Table 4 and 7). The flow chart of the whole procedure is illustrated in Figure 9.

5.1. *Crossmatch with LAMOST Multiple Epoch Data*

The LAMOST MRS multiple epoch catalog[11], released as part of LAMOST MRS DR10, contains spectroscopic observations of 547,726 targets obtained over multiple observation nights. Each target in the catalog

[11] http://www.lamost.org/dr10/v1.0/catalogue

Table 3. Kinematic and chemical properties of different Galactic components for the LAMOST-Gaia-TESS sample.

Components	N_s	N_p	V_tot	[Fe/H]	[α/Fe]	L_Z	$\sqrt{J_R}$	$\ln(J_Z)$	Age$_\mathrm{kin}$	Age$_\mathrm{zoomies}$
					MRS					
Thin disk	172,435	189	$35.0^{+22.4}_{-15.6}$	$-0.09^{+0.18}_{-0.22}$	$0.05^{+0.11}_{-0.07}$	1858^{+162}_{-160}	$4.3^{+3.0}_{-2.2}$	$1.1^{+1.2}_{-1.3}$	$2.60^{+0.16}_{-0.15}$	$1.41^{+2.37}_{-1.41}$
Thick disk	6,361	0	$101.2^{+29.2}_{-18.8}$	$-0.42^{+0.34}_{-0.28}$	$0.26^{+0.11}_{-0.16}$	1346^{+307}_{-208}	$11.3^{+3.6}_{-4.3}$	$3.3^{+0.8}_{-1.8}$	$13.04^{+1.84}_{-1.56}$	$9.73^{+4.27}_{-8.13}$
Halo	101	0	$238.54^{+63.90}_{-26.99}$	$-0.94^{+0.38}_{-0.73}$	$0.34^{+0.11}_{-0.07}$	320^{+189}_{-343}	$23.9^{+4.5}_{-2.7}$	$3.8^{+1.4}_{-1.7}$	NA	$10.25^{+3.75}_{-7.80}$
Sirius	5,569	5	$24.8^{+11.1}_{-9.3}$	$-0.10^{+0.17}_{-0.20}$	$0.06^{+0.11}_{-0.07}$	1927^{+27}_{-34}	$3.7^{+0.7}_{-0.5}$	$1.4^{+1.2}_{-1.3}$	NA	$2.20^{+4.09}_{-2.20}$
Hercules	3,532	7	$73.0^{+11.4}_{-17.9}$	$-0.10^{+0.25}_{-0.29}$	$0.09^{+0.17}_{-0.09}$	1466^{+45}_{-61}	$8.7^{+1.8}_{-2.0}$	$1.8^{+0.9}_{-1.1}$	NA	$2.79^{+3.93}_{-2.79}$
Pleiades/Hyades	3,162	1	$42.2^{+8.3}_{-5.9}$	$-0.08^{+0.21}_{-0.25}$	$0.08^{+0.12}_{-0.09}$	1568^{+89}_{-37}	$4.8^{+1.5}_{-1.0}$	$1.6^{+1.1}_{-1.2}$	NA	$2.76^{+4.15}_{-2.76}$
Coma	2,129	8	$19.8^{+7.3}_{-3.4}$	$-0.02^{+0.18}_{-0.21}$	$0.05^{+0.11}_{-0.08}$	1793^{+46}_{-54}	$1.7^{+0.7}_{-0.5}$	$0.8^{+1.4}_{-1.2}$	NA	$1.27^{+1.70}_{-1.27}$
γ Leo	591	0	$57.7^{+16.0}_{-17.1}$	$-0.15^{+0.22}_{-0.26}$	$0.10^{+0.11}_{-0.09}$	1900^{+50}_{-47}	$7.1^{+2.0}_{-1.3}$	$2.0^{+1.0}_{-1.3}$	NA	$4.29^{+5.56}_{-4.29}$
Wolf630	517	2	$34.2^{+5.4}_{-3.2}$	$-0.06^{+0.20}_{-0.24}$	$0.07^{+0.11}_{-0.08}$	1696^{+27}_{-41}	$3.2^{+0.5}_{-0.5}$	$1.2^{+1.2}_{-1.2}$	NA	$1.66^{+2.43}_{-1.66}$
HR1614	318	2	$71.3^{+7.1}_{-6.3}$	$-0.18^{+0.34}_{-0.33}$	$0.18^{+0.16}_{-0.15}$	1347^{+27}_{-32}	$8.8^{+0.7}_{-0.6}$	$2.1^{+1.1}_{-1.3}$	NA	$4.72^{+9.28}_{-4.72}$
Arcturus	268	0	$100.7^{+24.7}_{-6.6}$	$-0.46^{+0.38}_{-0.30}$	$0.28^{+0.12}_{-0.15}$	1118^{+27}_{-39}	$12.5^{+1.2}_{-0.8}$	$2.5^{+1.4}_{-1.3}$	NA	$6.31^{+7.69}_{-6.31}$
Dehnen	212	0	$51.35^{+4.2}_{-2.9}$	$-0.11^{+0.24}_{-0.21}$	$0.08^{+0.10}_{-0.08}$	1676^{+32}_{-28}	$5.5^{+0.6}_{-0.3}$	$2.6^{+1.3}_{-1.0}$	NA	$2.20^{+3.76}_{-2.20}$
A1/A2	139	0	$64.9^{+10.8}_{-9.3}$	$-0.35^{+0.31}_{-0.18}$	$0.12^{+0.10}_{-0.07}$	2185^{+22}_{-41}	$10.9^{+1.3}_{-0.5}$	$2.1^{+0.9}_{-1.3}$	NA	$4.36^{+6.53}_{-4.36}$
Antoja12	94	0	$96.5^{+8.3}_{-12.2}$	$-0.18^{+0.22}_{-0.28}$	$0.13^{+0.13}_{-0.10}$	1488^{+233}_{-51}	$9.9^{+1.6}_{-1.1}$	$2.1^{+0.9}_{-1.2}$	NA	$4.35^{+6.43}_{-4.35}$
ϵInd	20	0	$111.2^{+12.6}_{-4.4}$	$-0.40^{+0.56}_{-0.27}$	$0.21^{+0.19}_{-0.12}$	1261^{+25}_{-31}	$12.7^{+0.3}_{-0.9}$	$2.9^{+1.4}_{-1.4}$	NA	$7.97^{+6.03}_{-7.97}$

Note—See Table 2 for the units of each column.

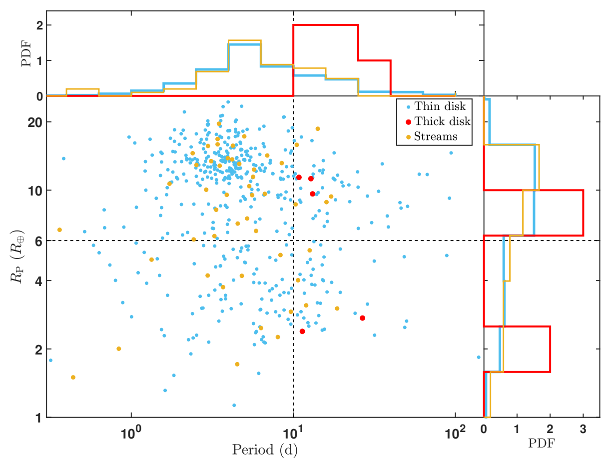

Figure 8. Planetary radius vs. orbital period for planets hosted by stars in different Galactic components. Planet candidates from both the LRS and MRS samples are shown. Different colors denote the Galactic components of the host stars, with planets in the thin disk, thick disk, and streams represented in blue, red, and orange, respectively. Two dashed lines highlight the classification criteria for different planet types: an orbital period of 10 days and a planetary radius of 6 $R_\oplus$. Histograms on the sides display the probability density functions (PDF) of planets in different components.

was typically observed with approximately 20 exposures spanning 5 observation nights. For each exposure of a given target, the catalog provides local modified Julian minute (lmjm), RV with associated errors, SNR and derived physical parameters (e.g., T_eff, $\log g$).

We first applied the following filtering procedures to the LAMOST MRS multiple epoch catalog: (1) We removed exposures with invalid RV measurements and errors. (2) We excluded exposures with SNR < 10, as the typical RV uncertainty for such measurements in the sample is approximately twice that of exposures with higher SNR, as indicated by Xiang et al. (2015). (3) Following our filtering process, some stars were left with fewer than two exposures across all observation nights.For each target, we calculated the total number of observation nights (N_{night}) and the number of exposures per night (n_i), where i denotes each observation night. To ensure reliability, we excluded observation nights with only one single exposure from the calculation of N_{night}, as such nights do not provide reliable information to assess RV variability. Stars with $N_{night} = 0$ were excluded from the sample. (4) Following a similar procedure described in Section 2, we applied filters on T_eff, [Fe/H], and [α/Fe] to ensure data quality and consistency. After applying these filters to the multiple epoch data, we cross-matched the remaining sample with Gaia and TESS catalogs, imposing a separation limit < 1.5 arcseconds and a magnitude difference < 2 in G-band magnitudes. Notably, we did not impose the RUWE threshold or RV consistency filter when constructing this sample, in order to retain potential RV variables and binary candidates. After applying these criteria, we obtained a final sample of 108,278 stars, including 114 TOI host stars. Each star in the dataset was observed between 2 and 150 times, with a typical value

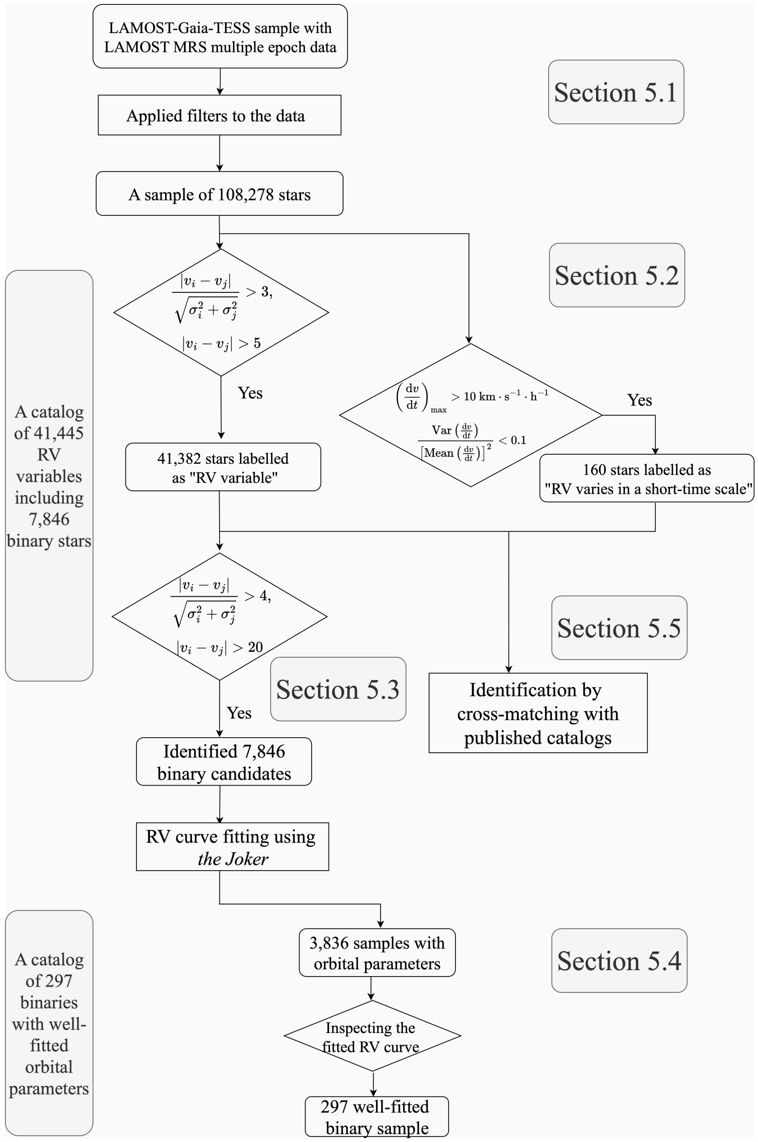

Figure 9. A summary flow chart of Section 5, with the corresponding subsection shown to the right of each process.

of 13 exposures. These observations are distributed over a time span of 2 to 37 days, typically covering around 3.5 nights.

5.2. *Identifying the RV Variables*

The identification of binary stars in our sample is based on detecting significant RV variations across multiple epochs. RV variability has been demonstrated to be a reliable diagnostic for identifying RV variables and estimating binary fractions in plenty of previous studies (Badenes & Maoz 2012; Maoz et al. 2012; Price-Whelan et al. 2018, 2020; Mahy et al. 2022, additional references below). One common approach classifies a star as a binary if its RV shows statistically significant variability, being assessed using χ^2 probability that the RV is constant (Latham et al. 2002; Carney et al. 2003; Hansen et al. 2016a,b), or assessed through comparing the maximum RV shift to measurement uncertainties and/or applying a minimum threshold (Sana et al. 2013, 2012; Badenes et al. 2018; Mazzola et al. 2020). These methods can also derive the intrinsic binary fraction and has been adopted in large-scale analyses of various stellar populations (Dunstall et al. 2015; Moe et al. 2019; Luo et al. 2021; Guo et al. 2022; Guo et al. 2022; Daher et al. 2022; Bonidie et al. 2022). Instead of identifying individual systems, another approach focuses on population-level inference of the overall binary fraction. It infers binary fraction statistically from the dispersion in RVs across multi-epoch observations (e.g., Gao et al. 2014, 2017; Tian et al. 2018). More recent work of Bashi & Tokovinin (2024); Bashi et al. (2024); Bashi & Belokurov (2025) modeled the RV variation distribution as a mixture of single and binary populations, enabling binary fraction estimates without resolving each binary's orbit. This approach enable efficient, homogeneous estimation of binary fractions across large samples.

In this work, we aim to construct a stellar catalog and characterize the kinematic properties and binarity of the sample, with the additional goal of deriving orbital parameters for selected binary systems. To this end, we focus on identifying binary stars on a star-by-star basis using the first approach described above. To identify RV variables and binary candidates, we adopted the method described by Sana et al. (2012, 2013), which evaluates the significance of RV variations through Equation 2. We conducted a Monte-Carlo simulation accounting for LAMOST's observational cadence and measurement uncertainty to determine the threshold in Equation 2 by evaluating the completeness and purity (see Section 5.3). For the identified binaries, we fit their RV curves using *The Joker* package (Price-Whelan et al. 2017, 2018), enabling us to obtain binary orbital properties and construct a catalog of well-characterized binaries (see Section 5.4).

Specifically, a star is classified as an RV variable or a binary candidate if at least one pair of RV measurements satisfies both of the following criteria simultaneously:

$$\begin{aligned} \frac{|v_i - v_j|}{\sqrt{\sigma_i^2 + \sigma_j^2}} &> A, \\ |v_i - v_j| &> C, \end{aligned} \tag{2}$$

where v_i and v_j are the RV measurements of the same star from two different exposures, and σ_i and σ_j are their uncertainties.

The first criterion in Equation 2 evaluates the significance of RV variations, while the second criterion imposes a minimum amplitude threshold C to exclude small yet statistically significant variations. Here, we set thresholds of $A = 3$ and $C = 5$ km s^{-1} to ensure that the detected RV variations are statistically significant. These criteria help distinguish RV changes likely caused by binary motion or intrinsic stellar variability from those resulting from instrumental noise or measurement limitations. Following Tian et al. (2020), we classify these stars as 'RV variables', which include potential binary systems as well as intrinsically variable stars. Applying the two criteria, we identified 41,382 RV variables in our sample.

Moreover, previous studies have shown that stellar activity can also produce significant RV variations. For instance, photospheric variations in supergiants can mimic RV variations with amplitudes of up to 20 km s^{-1} (Ritchie et al. 2009), and stellar wind effects can also contribute to such variations (Li et al. 2016). Therefore, the second criterion is particularly important when identifying binary stars, and the selection of threshold values A and C for binary identification will be further discussed in Section 5.3.

In addition to targets with observation coverage spanning multiple nights, 31,639 stars were observed on only a single night ($N_{\rm night}$=1), accounting for approximately 30% of the total sample. Some of these targets may display rapid RV variations over short periods, such as compact objects (Liu et al. 2024). To address this limitation, we introduced a new classification flag, 'Short Time Scale RV Variable', specifically designed to capture significant RV variation within a short time span. We calculated the rate of RV change (dv/dt) between consecutive observations within a single night, along with the variance of these rates. Only nights with at least three exposures were considered, ensuring at least two dv/dt measurements.

Following Liu et al. (2024), we select stars whose dv/dt values satisfy the following conditions:

$$\begin{aligned} &\left(\frac{\mathrm{d}v}{\mathrm{d}t}\right)_{\max} > 10\ \mathrm{km}\cdot\mathrm{s}^{-1}\cdot\mathrm{h}^{-1}, \\ &\frac{\mathrm{Var}\,(\mathrm{d}v/\mathrm{d}t)}{\left[\mathrm{Mean}\,(\mathrm{d}v/\mathrm{d}t)\right]^2} < 0.1 \end{aligned} \tag{3}$$

Applying these criteria, we identified 160 stars in our sample as 'Short Time Scale RV Variables', increasing the total number of RV variables in the LAMOST-Gaia-TESS catalog to 41,445.

5.3. *Identifying the Binaries*

In order to further confirm the values for A and C (Equation 2) for binaries, we employ a Monte Carlo approach to quantify their impacts on the detection purity (i.e, the proportion of identified binary candidates that are indeed true binary systems).

In the simulation, we generate a synthetic stellar population of 10^5 systems, consisting of 45% single stars and 55% binaries, based on the median binary fraction from LAMOST (Tian et al. 2020). For the binary population, we assume the following distributions for key orbital parameters:

1. **Mass Ratio (q) :** Follows a power-law distribution $p(q) \propto q^{\gamma}$, where the index γ is 1.16 ± 0.16 for short period binaries with $\log P < 5.5$ and -0.01 ± 0.03 for binaries with larger periods, as suggested by Duchêne & Kraus (2013).

2. **Orbital Period (P) :** Adopts a log-normal distribution characterized by a mean value of $\mu_{\log P}$

= 5.03 and a dispersion of $\sigma_{\log P} = 2.28$ (Raghavan et al. 2010), with P expressed in days.

3. **Eccentricity (e) :** Assumed to follow a uniform distribution in the range [0, 1], alternative distributions were tested and yielded similar results.

The synthetic populations are generated as follows:

1. Each star in the synthetic population is assigned an observation list that includes the number of observation nights ($N_{\rm night}$), the number of exposures per night (n_i), and the corresponding RV measurement errors from the observed dataset (σ_i).

2. For the single stars, each is assigned an RV measurement along with the uncertainty from the multiple epoch catalog described in Section 5.1. The RVs at the corresponding observation times are drawn from Gaussian distributions centered on their assigned RV measurements.

3. For binary stars, the three-dimensional orbital orientation and the time of periastron passage are drawn randomly from 0 to 2π. The orbital period (P), mass ratio (q), and eccentricity (e) are also drawn randomly according to the distributions specified earlier. The RVs of the primary stars are then computed at the each observation epoch based on the orbital parameters using

$$RV_0 = \sqrt[3]{\frac{2\pi G}{P(1-e^2)^{\frac{2}{3}}}\frac{(M\sin i)^3}{(M_*+M)^2}}\cos\left(\omega + \frac{2\pi t}{P}\right) \quad (4)$$
$$RV \sim \mathcal{N}(RV_0, err_{RV})$$

We further evaluated the performance of our binary detection criteria on the mock sample by varying the thresholds (A, C) in Equation 2. Specifically, we explored different cutoffs for $\Delta{\rm RV}/\sigma_{\rm RV}$, selecting values of 2, 3, and 4, as well as various values for the constant C, ranging from 5 to 20 km s^{-1}. For each combination of (A, C), synthetic stars, regardless of whether single or binary, were flagged as binaries if they satisfied the criterion in Equation 2. To minimize the effect of random sampling fluctuations, we repeated the above process for 10 times and adopted the average value of detection purity. The results, including the detection rate (i.e., the fraction of binary stars detected from the 55,000 true binary systems) and the corresponding purity, are summarized in Table 5.

Based on our simulation results, we adopt thresholds of $A = 4, C = 20$ km s^{-1} in Equation 2 to identify binary stars with higher purity while minimizing contamination from intrinsic stellar variability, as discussed in the previous section. These thresholds yield a 100% purity in eliminating single star contamination (Table 5). However, it is important to note that this purity represents an upper bound, as we have not accounted for the effects of intrinsic stellar variability (e.g., eruptive stars, pulsating stars) that may affect the identification process.

Additionally, we require that each star be observed on at least two separate nights ($N_{\rm night} \geq 2$) to ensure that the RV measurements span enough of the orbital phases, enabling effective RV curve fitting (discussed later in Section 5.4). Applying these stricter criteria, we classified 7,846 stars as binaries among the RV variables in our catalog.

Figure 10 illustrates the detection efficiency and the distribution of mass ratio and orbital period for the detected binaries in the simulated sample, based on the adopted thresholds of A = 4, C = 20 km s^{-1}. As shown, our detection method is primarily sensitive to binaries with orbital periods shorter than 10^3 days, a limitation arising from the observational strategy and the time baseline of the LAMOST survey. The results highlight the survey's inherent sensitivity toward detecting short-period binaries, which tend to exhibit more pronounced and periodic RV variations within the time span.

Table 4. The catalog of the LAMOST multiple epoch sample

Column	Name	Format	Units	Description
Parameters obtained from Gaia, LAMOST and TESS (41,445 rows)				
1	Gaia DR3 ID	Long		Unique Gaia source identifier
2	LAMOST ID	String		LAMOST unique spectral ID
3	TIC	Integer		TESS Input Catalog (TIC) ID
4-37	⋮			Columns 4-37 from Table 2

Table 4 *continued*

Table 4 *(continued)*

Column	Name	Format	Units	Description
38	$N_{\rm p}$	Integer		Planet (candidate) multiplicity
39	Full TOI ID	String		Unique TESS Object of Interest identifier
40	LAMOST obsid list	String		Spectrum ID for each observation of the target from LAMOST
41	Exposure number	Float		Total exposure number for the target from LAMOST
42	RV list	String	km s^{-1}	Radial velocity list ('rv_b1_list' from LAMOST)
43	e_RV list	String	km s^{-1}	Corresponding uncertainty of radial velocity
44	SNR list	String		S/N for each exposure from LAMOST
		Parameters derived from multiple epoch data (41,445 rows)		
45	N_{night}	Short	days	Number of effective observation nights
46	N_i	String	days	Number of exposures for each observation night
47	Delta exposure	Double	days	Time interval between exposures
48	T_{max}	Double	minutes	Time span for the target
49	Delta_RV_max	Double	km s^{-1}	Maximum RV difference for each target
50	RV Variable	Boolean		True if satisfies the criteria for variable flag in Section 5.2
51	Short time scale RV variable	Boolean		True if satisfies the criteria for short time scale flag in Section 5.2
52	Binary	Boolean		True if satisfies the criteria for binary flag in Section 5.2
		Cross-match flag and results (41,445 rows)		
53	Gaia_VCR_flag	Boolean		True if included in Gaia DR3 variabe catalog
54	Class_Gaia	String		Gaia classification
55	VSX_flag	Boolean		True if included in VSX
56	Period_VSX	Double	days	Variable star period from VSX catalog
57	Type_VSX	String		Variability type from VSX catalog
58	Name_VSX	String		Variable star identifier from VSX catalog
59	GCVS_flag	Boolean		True if included in GCVS
60	Type_GCVS	String		Variability type from GCVS
61	Name_GCVS	String		Variable star identifier from GCVS
62	Period_GCVS	Double	days	Variable period from GCVS
63	ASAN-SN_variable_flag	Boolean		True if included in ASAN-SN_variable
64	Type_ASAN-SN_variable	String		Variability type from ASAN-SN_variable catalog
65	Period_ASAN-SN_variable	Double	days	Variable period from ASAN-SN_variable catalog
66	ASAN-SN_binary_flag	Boolean		True if included in ASAN-SN_binary catalog
67	Period_ASAN-SN_binary	Double	days	Binary period from ASAN-SN binary catalog
68	TESS EB_flag	Boolean		True if included in TESS EB catalog
69	NSS_SB1_flag	Boolean		True if included in Gaia-NSS SB1 catalog
70	Period_NSS_SB1	Double	days	Binary period from Gaia-NSS SB1 catalog
71	NSS_EB_flag	Boolean		True if included in Gaia-NSS EB catalog
72	Period_NSS_EB	Double	days	Binary period from Gaia-NSS EB catalog
73	NSS_astrometry_flag	Boolean		True if included in Gaia-NSS Astrometry catalog
74	Period_NSS_astrometry	Double	days	Binary period from Gaia-NSS Astrometry catalog
		Parameters derived from fitting the radial velocity curve (7,846 rows)		
75	P_unimodal	Boolean		True if period is well constrained
76	P_bimodal	Boolean		True if period is bimodal
77	Period joker	String	days	Period calculated from *The Joker*, two values if period is bimodal
78	eccentricity	Double		Eccentricity from *The Joker*
79	K	Double	km s^{-1}	Semi-amplitude from *The Joker*
80	v_0	Double	km s^{-1}	System barycentric velocity from *The Joker*
81	ω	Double	rad	Argument of pericenter from *The Joker*

Table 4 *continued*

Table 4 *(continued)*

Column	Name	Format	Units	Description
82	M_0	Double	rad	Mean anomaly from *The Joker*
83	$f(m)$	Double	$M_\odot$	Derived mass function
84	M_{comp}	Double	$M_\odot$	Lower limit of companion mass
Kinematic properties for binaries (3,836 rows)				
85	R	Double	kpc	Galactocentric Cylindrical radial distance
86	θ	Double	deg	Galactocentric Cylindrical azimuth angle
87	Z	Double	kpc	Galactocentric Cylindrical vertical height
88	$U_{\rm LSR}$	Double	km s^{-1}	Cartesian Galactocentric x-velocity to the LSR
89	$V_{\rm LSR}$	Double	km s^{-1}	Cartesian Galactocentric y-velocity to the LSR
90	$W_{\rm LSR}$	Double	km s^{-1}	Cartesian Galactocentric z-velocity to the LSR
91	L_X	Double	kpc km s^{-1}	Galactocentric x-angular momentum
92	L_Y	Double	kpc km s^{-1}	Galactocentric y-angular momentum
93	L_Z	Double	kpc km s^{-1}	Galactocentric z-angular momentum
94	J_R	Double	kpc km s^{-1}	Radial orbital action
95	J_Z	Double	kpc km s^{-1}	Vertical orbital action
96	t_{J_Z}	Double	Gyr	kinematic age derived from J_Z using *zoomies*
97	$t_{J_Z}^{Up}$	Double	Gyr	1-σ upper limit of kinematic age derived from J_Z using *zoomies*
98	$t_{J_Z}^{Lower}$	Double	Gyr	1-σ lower limit of kinematic age derived from J_Z using *zoomies*
99	TD/D	Double		Thick disc to thin disc membership probability
100	TD/H	Double		Thick disc to halo membership probability
101	$Herc/D$	Double		Hercules stream to thin disc membership probability
102	$Herc/TD$	Double		Hercules stream to thick disc membership probability
103	Component	String		Classification of Galactic components

NOTE—Table 4 is published in its entirety in the machine-readable format. A column description is shown here for guidance regarding its form and content.

5.4. *Binary Orbital Parameters from Radial Velocity Curve Fits*

In this subsection, we present the radial velocity curve fitting procedure for the 7,846 binary candidates. Given the sparse and non-uniform RV data, we employed the Python package *The Joker* to derive orbital parameters (e.g. period P, eccentricity e, semi-amplitude K) for our identified binary candidates from the multiple-epoch RV data. *The Joker* is a custom Markov Chain Monte Carlo (MCMC) sampler specifically designed to handle non-uniform datasets and can search over orbital parameter space for likely orbits (Price-Whelan et al. 2017). It has been widely used in large sample surveys for statistical analysis of binary orbital posteriors from RV curves, such as APOGEE (Price-Whelan et al. 2018), MUSE (Giesers et al. 2019), as well as in exoplanet detection through RV data (Rosenthal et al. 2021).

The RV fitting procedure is described as follows: we first fitted the RV curve with a Keplerian orbit in the form of six parameters, that is:

$$v(t;\boldsymbol{\theta}) = v_0 + K[\cos(\omega + f) + e\cos\omega], \quad (5)$$

where v_0 is the barycentric velocity (center-of-mass RV), K is the semi-amplitude of the RV curve, f is the true anomaly which can be derived from mean anomaly M, ω is the argument of periastron, and e is the eccentricity. For each of the 7,846 binary candidates, we ran *The Joker* to generate posterior samplings for the Keplerian orbital parameters. We began by generating a cache of 20,000,000 prior samples for the nonlinear parameters, which were drawn from the prior probability density functions (PDFs) summarized in Table 6, where σ_K is defined by Equation 6 using σ_K = 15 km s^{-1}, P_0 = 365 days, following Price-Whelan et al. (2018):

$$\sigma_K = \sigma_{K,0}\left(\frac{P}{P_0}\right)^{-1/3}\left(1-e^2\right)^{-1/2} \quad (6)$$

After sampling with *The Joker*, we identified 3,836 binary systems exhibiting a unimodal orbital solution with determined parameters (hereinafter referred to as the unimodal sample). For these binaries, we derived the

Table 5. Detection Rate and Purity for different ΔRV thresholds and C values.

C (km s^{-1})	$\Delta RV > 2\sigma$		$\Delta RV > 3\sigma$		$\Delta RV > 4\sigma$	
	Detection Rate	Purity	Detection Rate	Purity	Detection Rate	Purity
5	0.3373	0.6024	0.2045	0.6946	0.1131	0.9460
10	0.1040	0.8969	0.0999	0.9269	0.09216	0.9828
15	0.0708	0.9898	0.0706	0.9923	0.0704	0.9974
20	0.0557	0.9977	0.0556	0.9983	0.0556	1.0000

Table 6. Summary and Description of Priors

Name	Prior	Description
P	$p(P) \propto \frac{1}{P}; P \in (0.2, 10000)$ day	Period
e	$e \sim \mathrm{Beta}(0.867, 3.03)$	Eccentricity
M_0	$M_0 \sim \mathcal{U}(0, 2\pi)$ rad	Mean anomaly at reference time
ω	$\omega \sim \mathcal{U}(0, 2\pi)$ rad	Argument of pericenter
K	$K \sim \mathcal{N}(0, \sigma_K)$ km s^{-1}	Velocity semi-amplitude
v_0	$\mathcal{N}\left(0, 100^2\right)$ km s^{-1}	System barycentric velocity

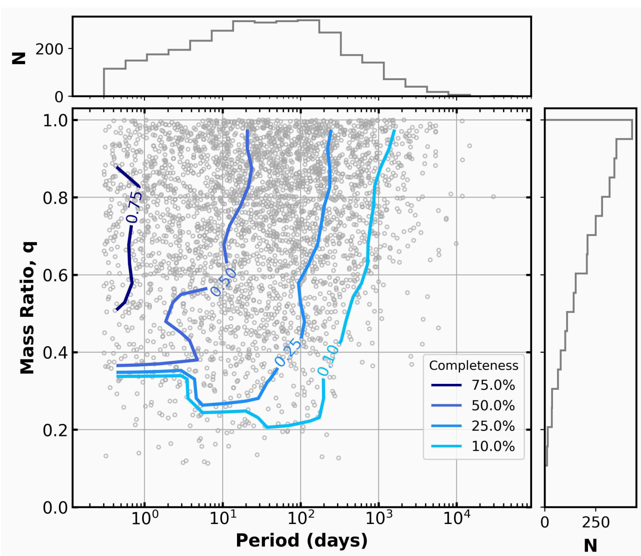

Figure 10. Distribution of binary mass ratio (q) and orbital period (P) for the simulated binaries which were retrieved by the detection method. Different detective completeness contour lines were plotted on the period-mass ratio plane. Histograms of q and period were shown on the top and right side of the figure.

binary mass function $f(M)$ following Equation 7 using the posterior samples from our RV modeling:

$$f(M) = \frac{M_1 q^3 \sin^3 i}{(1+q)^2} = \frac{PK^3\left(1-e^2\right)^{3/2}}{2\pi G}, \qquad (7)$$

where M_2 is the mass of the invisible star, $q = M_2/M_1$ is the mass ratio, i is the system inclination angle, K is the RV semi-amplitude of the visible star and P is the orbital period. Using this mass function, we estimated the lower limit of the companion's mass under the assumption of $i = 90°$ (See Column M_{comp} in Table 4).

The remaining 4,010 systems failed to yield well-determined periods due to insufficient sampling. Among them, 561 systems exhibited two distinct period modes, indicating that one or a few additional radial velocity measurements would be sufficient to uniquely determine their orbits, as noted by Price-Whelan et al. (2018).

For systems with a unique orbit solution, we generated additional prior samples to mitigate sampling limitations and utilized the posterior samples returned by *The Joker* to initiate an MCMC process for deriving the posterior distribution. We visually inspected the inferred orbital solutions and the resulting RV curves for all systems in this sample, flagging those with questionable or invalid fits (an example RV curve is shown in Figure B1). After filtering out poorly fitted RV curves (e.g., those lacking significant periodic variations), we retained a subset of 297 binary stars with well-folded RV curves (hereinafter referred to as the well-fitted sample), which is presented in Table 7.

For the fitted binary sample, we calculated spatial velocities and angular momenta using the fitted systemic velocities, and determined their Galactic components following the procedure described in Section 3. We found that 91.3±1.6% of the binaries belong to the thin disk, a significantly higher fraction than in the single star sample (83.0±0.1%), while only small fractions are in the thick disk (1.7%) and stellar streams (1.3%). This distribution suggests the binary population may be preferentially found in the younger thin disk component.

Figure 11 illustrates the relationship between orbital periods and semi-amplitudes for stars in the unimodal

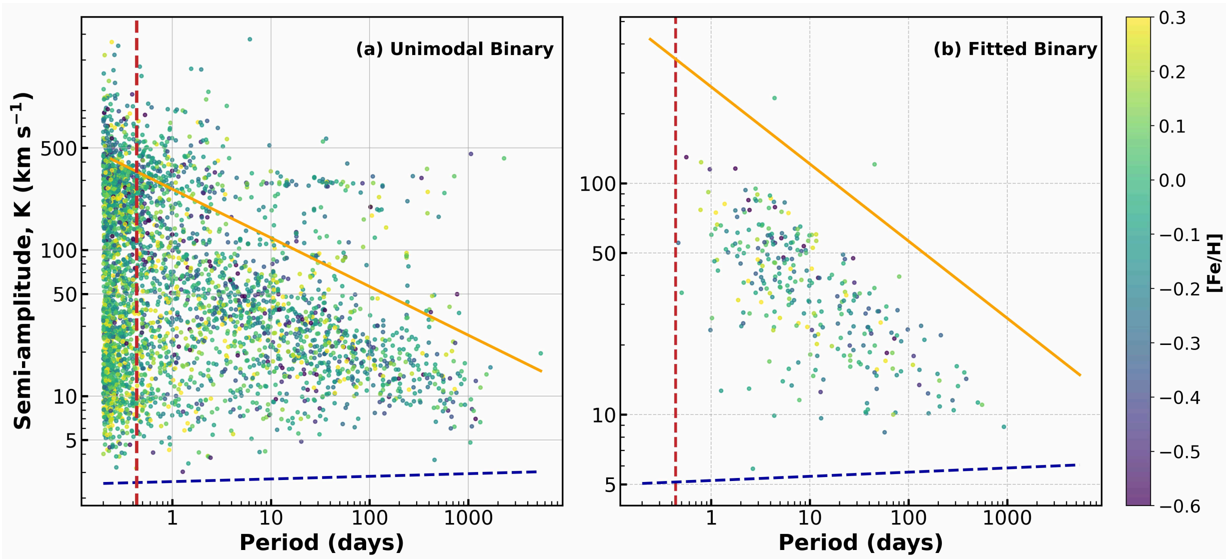

Figure 11. Left: Inferred semi-amplitude K vs. orbital periods for the binary samples, color-coded by [Fe/H]. The left panel shows the 3,836 binaries with unimodal samplings, while the right panel shows the 297 well-fitted samples. The three colored reference lines, from top to bottom, represent the following: The bottom dashed blue line corresponds to the $\Delta RV > 4\sigma$ threshold, used to distinguish significant RV variations. The left red dashed line indicates the lower limit of the period calculated from the Roche limit. The top orange line represents a rough estimation of upper limit for the semi-amplitude K.

sample (left panel) and the well-fitted sample (right panel). We found that the majority of our binary stars are short-period binaries, commonly referred to as close binaries (Moe & Di Stefano 2017), with a typical orbital period of 7.5 days.

Notably, a significant fraction of stars in the unimodal sample exhibit short orbital periods of less than 0.5 days. Among these, some display large mass ratios, suggesting potential inaccuracies in the derived parameters. Such discrepancies may result from sparse RV sampling or low-quality data and could also in turn affect the reliability of the inferred kinematics. To assist in evaluating the reliability and physical plausibility of the data, we have added three reference lines in Figure 11, which serve as benchmarks for further scrutiny.

The bottom line represents the 4σ threshold for RV variations, as determined by our selection criteria outlined in Section 5.2. This threshold reflects the minimum RV amplitude required for a star to be classified as a binary in our sample.

The vertical red line marks the lower limit for orbital periods as the binary will fill its Roche lobe below a critical distance. Using

$$a_R = (\frac{R_p}{0.462})(\frac{M_*}{M_p})^{\frac{1}{3}} \quad \text{(Faberet al. 2005)}, \qquad (8)$$

we derive a reference period of 0.436 days by adopting $R_{comp} = 0.8\,R_{median}$ and $M_{comp} = 0.8\,M_{median}$, where R_{comp} and M_{comp} are the radius and mass of the unseen companion, while R_{median} and M_{median} represent the typical values of the primary star.

The top line indicates an upper limit for the RV semi-amplitude, derived from the mass function $f(M)$ (Equation 7) under the assumption of a circular orbit ($e = 0$). The constraint for K is given by:

$$K \leq \frac{f(M)}{1.0361 \times 10^7} \left(\frac{P_{\rm orb}}{\rm days}\right)^{-1} (\,\rm km\ s^{-1}) \qquad (9)$$

As shown in the right panel of Figure 11, the majority of stars in the well-fitted sample reside within the region defined by these reference lines. This alignment indicates that our fitting method is robust and effective in identifying binaries with realistic orbital parameters, ensuring reliability and consistency in the derived results.

Figure 12 displays the orbital period as a function of eccentricity (left panel) and mass ratio (right panel) for the well-fitted sample. As illustrated, the q-P distribution reveals a peak in q around 0.3-0.5, while also displaying sparsely populated region in both the upper-left and upper-right corners of the right panel. In addition to the selection bias caused by the LAMOST observational cadence and time baseline, limiting our ability to detect binaries with either very short or long periods (P > 1000 days). Systems with low mass ratios are also more likely to be missed due to their smaller RV amplitudes being lost in the noise. Moreover, in cases where an SB2 system is misclassified as a single-lined spectroscopic binary, the companion's spectral contribution may blend with that of the primary, potentially biasing the observed RV amplitudes toward lower values and resulting in underestimated mass ratios (Joergens et al. 2010), thereby reducing the number of detected high-q systems. Beyond selection effects, the lack of systems in the upper-left (short-period, high-q systems) and upper-right (long-period, high-q systems) regions of the q-P distribution may also reflect physical mechanisms. For instance, short-period, high-q binaries may undergo orbital evolution due to tidal dissipation (Zahn 1975, 2008; Mazeh 2008; Offner et al. 2023). The observed deficit of high-q binaries with intermediate periods (20–500 days) may be linked to the intrinsic properties of early-type binaries, as suggested by Moe & Di Stefano (2017).

The positive correlation observed between q and period may be partially influenced by selection effects, as long-period systems with low q are more difficult to detect (see Figure 10). Meanwhile, the positive correlation between e and period in the left panel demonstrates the impact of tidal circularization (Meibom & Mathieu 2005; Mazeh 2008; Zahn 2008), with eccentricities of systems having $P < 10$ days being more concentrated near $e = 0$, compared to those with longer orbital periods, this trend has been observed across various samples (Raghavan et al. 2010; Price-Whelan et al. 2018; Windemuth et al. 2019; Price-Whelan et al. 2020; Kounkel et al. 2021; Chen et al. 2023; Guo et al. 2025). The dotted line in Figure 12 represents the upper envelope adopted from Mazeh (2008), which was derived from 2,751 binary systems in the 9th Catalog of Spectroscopic Binaries (Pourbaix et al. 2004). As shown, the majority of our sample resides within the envelope while only a few stars exceed above the envelope, similar trend has also been reported in LAMOST LRS sample (Chen et al. 2023). For these outliers above the envelope, the elevated eccentricities may be linked to their relatively high effective temperatures (typically exceeding 6,250 K), or they may reflect long-term RV trends suggestive of a third body. Alternatively, these deviations could also be attributed to high primordial eccentricity. Nevertheless, the precise origin of these outliers remains uncertain.

Despite being widely observed, the underlying mechanisms of the positive e-p correlation still remains an open question. Meibom & Mathieu (2005) introduced the concept of 'circularization period' (P_{circ}), defined as the period below which most binaries appear to be circular. Subsequent studies found that P_{circ} increases with stellar age (Meibom & Mathieu 2005; Meibom et al. 2006; Geller & Mathieu 2012; Milliman et al. 2014; Leiner et al. 2015; Nine et al. 2020; Geller et al. 2021, e.g.,), indicating active tidal circularization throughout the main-sequence phase and providing constraints the tidal theories (Zahn 1975, 1989; Zahn & Bouchet 1989; Ogilvie & Lin 2007). Nevertheless, Zanazzi (2022) suggested the apparent age dependence of P_{circ} may be influenced by a 'cold core', and highlighted the role of resonance locking in addition to equilibrium and dynamical tides. In contrast, other studies using large samples of eclipsing binaries have found that the eccentricity distribution also varies with stellar temperature: the circularization period decreases with increasing temperature, with hotter binaries tend to be more eccentric at shorter periods (Van Eylen et al. 2016; Triaud et al. 2017; Justesen & Albrecht 2021; IJspeert et al. 2024). By analyzing spectroscopic binaries, Bashi et al. (2023) found the dependence of cutoff period on age is not significant comparing with the dependence on temperature. These observations indicate that equilibrium tides may dominate tidal circularization in the pre-main-sequence, while additional effective mechanisms likely contribute to tidal evolution at later stages (Khaliullin & Khaliullina 2011; Barker 2022).

To uncover the process of tidal evolution in binary systems, it is essential to disentangle how properties such as circularization period vary with stellar age, metallicity, and other parameters individually. However, this task is complicated by the strong correlations among stellar properties (e.g., age, temperature, metallicity). In this work, we construct a large catalog of binaries with orbital parameters, stellar parameters, as well as kinematic age estimates, offering a solid foundation for such investigations. Based on this catalog, by controlling for confounding parameters, one can examine the temporal evolution of binary characteristics (e.g., orbital eccentricity, mass ratio), thereby shedding light on the mechanisms driving tidal circularization of binary systems (to be discussed in a follow-up paper, Wu et al. in prep.).

5.5. *Characteristics of the RV Variable Catalog*

In the above Sections, we have identified 41,445 RV variables, including 7,846 binaries including a sample of 297 systems with well-constrained orbits (summarized as in Figure 9 and Table 8). However, as noted in Section 5.3, in addition to stellar activity such as photospheric variations that can produce significant RV shifts, the binary catalog may also be contaminated by intrinsically variable stars. Specifically, pulsating stars such as Cepheids, e.g., δ Cephei (10–50 km s^{-1}, Ripepi et al. 2023; Anderson et al. 2024), Mira variables (5–20 km s^{-1}, Samus' et al. 2017), and RR Lyrae stars (up to 50–100 km s^{-1}, Bono et al. 2020; Clementini et al. 2023; Wang et al. 2024) can exhibit RV amplitudes comparable to those of binaries. Eruptive or active stars, in-

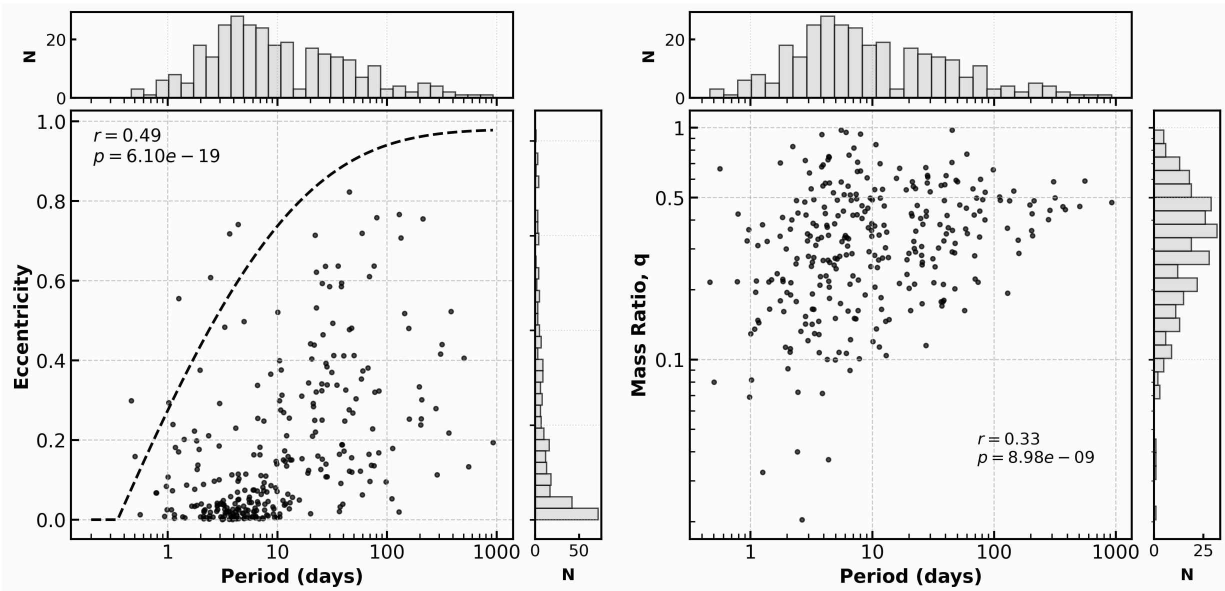

Figure 12. Orbital eccentricity (left panel) and binary mass ratio (right panel) as functions of orbital period for the well-fitted binary samples. Both parameters show positive correlations with orbital period, with Pearson correlation coefficients of 0.48 and 0.33, respectively, and p-values < 0.05. Dotted lines in the left panel is the upper envelope from Mazeh (2008). On the eccentricity-period plane, the well-fitted sample shows a concentrated distribution of eccentricities across all periods, with a tendency for lower eccentricities at shorter periods indicating tidal circularization effort.

cluding T Tauri and FU Orionis types, may also induce RV shifts of up to ~ 5 km s^{-1} due to accretion shocks, jets, or chromospheric activity (Szabó et al. 2021). To further validate the identified binaries and characterize the remaining variables, we performed cross-match with the following variable star and binary star catalogs:

1. ***VSX Catalog***[12]: The International Variable Star Index (VSX) is a comprehensive, continuously updated database maintained by the American Association of Variable Star Observers (AAVSO). It includes detailed information such as their variability types, periods, and amplitudes Watson et al. (2006) on approximately 2,280,000 variable stars.

   We cross-matched the VSX database with our sample and identified a total of 1,138 matched targets, which are composed of eclipsing binaries (32.6%), pulsating variables (42.88%), rotating variables (21.44%) and eruptive and other variable types (0.73%). Among the 371 eclipsing binaries, 263 sources are identified as binary stars in our RV variable catalog.

2. ***Gaia DR3 Variable Catalog*** [13]: The Gaia DR3 classifies 9,976,881 sources into 24 variability classes using supervised machine learning (Eyer et al. 2023). These variables are mainly composed of pulsation, rotation, and eclipsing systems, accounting for 34%, 28%, and 22%, respectively.

   The cross-match with our radial velocity (RV) variable star catalog yielded 2,605 common sources, including 1,216 rotating variables (such as RS Canum Venaticorum, α^2 CVn, and stars with solar-like variability), 1,085 pulsating variables (e.g., δ Scuti, γ Doradus), 296 eclipsing binaries, 1 RR Lyrae star, 6 young stellar objects, and 2 exoplanetary transits. Among the 296 eclipsing binaries, 218 were identified as binary stars in our catalog.

3. ***GCVS*** [14]: The General Catalog of Variable Stars (GCVS) is a comprehensive database of variable stars, maintained by the Sternberg Astronomical Institute at Moscow University. The fifth edition (GCVS 5.1) contains 58,202 individually identified and named variable stars (Samus' et al. 2017).

   Our RV variable catalog overlaps with GCVS 5.1 for 107 sources, including 81 eclipsing binaries, 7 δ Scuti stars, 14 eruptive variables (e.g., UV Ceti), 4 rotational variables, and 1 RR Lyrae star. Of the 81 eclipsing binaries, 61 were classified as binary stars in our catalog.

[12] https://www.aavso.org
[13] https://gea.esac.esa.int/archive/
[14] https://heasarc.gsfc.nasa.gov/W3Browse/all/gcvs.html

Table 7. Catalog of 297 Well Fitted Binary

TIC	Gaia DR3 ID	Period	e	K	v_0	ω	M_0	$M_{\rm comp}$	$P_{\rm mcmc}$	$e_{\rm mcmc}$	$K_{\rm mcmc}$	$v_{0\ \rm mcmc}$	$\hat{R}$
-	-	(days)	-	(km s^{-1})	(km s^{-1})	(rad)	(rad)	($M_\odot$)	(days)	-	(km s^{-1})	(km s^{-1})	-
1	2	3	4	5	6	7	8	9	10	11	12	13	14
60288033	609809150428649472	307.90	0.42	16.19	21.76	0.62	1.08	0.77	$307.92^{+0.10}_{-0.10}$	$0.41^{+0.01}_{-0.01}$	$16.29^{+0.28}_{-0.25}$	$21.63^{+0.20}_{-0.19}$	1.00
63209649	2126356983051726720	4.43	0.05	78.88	-17.71	0.57	0.30	0.87	$4.71^{+0.43}_{-0.87}$	$0.54^{+0.23}_{-0.18}$	$83.53^{+31.71}_{-9.29}$	$-8.74^{+12.00}_{-7.20}$	6.67
1001066189	1505618931851239552	12.13	0.21	22.26	3.31	1.91	0.50	0.27	$12.13^{+0.02}_{-1.60}$	$0.23^{+0.52}_{-0.02}$	$22.17^{+16.89}_{-0.32}$	$3.20^{+0.31}_{-6.61}$	1.58
276662038	3217291698571122816	11.58	0.02	28.87	19.78	3.86	-0.51	0.36	$11.94^{+0.39}_{-1.18}$	$0.40^{+0.33}_{-0.09}$	$27.19^{+27.59}_{-3.75}$	$14.22^{+6.85}_{-8.62}$	3.35
99236062	1009391604610898176	5.40	0.02	47.80	73.90	-2.76	1.03	0.28	$5.62^{+0.41}_{-0.39}$	$0.83^{+0.13}_{-0.22}$	$47.13^{+41.82}_{-9.45}$	$73.34^{+5.48}_{-7.61}$	6.07
46361693	608190188275369728	13.71	0.06	14.18	92.77	2.63	2.74	0.15	$13.96^{+0.46}_{-0.77}$	$0.40^{+0.38}_{-0.10}$	$13.89^{+3.27}_{-2.25}$	$94.13^{+2.88}_{-2.97}$	3.35
46305454	604943639676920448	207.22	0.30	10.85	-3.27	2.72	-1.06	0.34	$207.22^{+0.10}_{-0.10}$	$0.30^{+0.03}_{-0.03}$	$10.59^{+0.35}_{-0.35}$	$-3.26^{+0.24}_{-0.24}$	1.00
60392646	3419723643353175808	6.69	0.04	55.58	-49.76	1.96	0.64	0.67	$6.49^{+0.94}_{-0.42}$	$0.66^{+0.18}_{-0.19}$	$67.32^{+16.96}_{-10.46}$	$-35.12^{+21.24}_{-19.75}$	5.84
46361691	608189290627289856	0.79	0.07	123.33	61.19	2.44	-1.70	0.43	$1.00^{+0.50}_{-0.46}$	$0.74^{+0.16}_{-0.15}$	$104.34^{+26.79}_{-20.28}$	$33.68^{+9.44}_{-12.08}$	7.13
165624130	1612920305965260032	8.20	0.01	50.91	4.94	4.66	2.54	0.41	$8.56^{+0.32}_{-1.08}$	$0.70^{+0.15}_{-0.30}$	$50.13^{+27.48}_{-13.58}$	$-5.30^{+10.66}_{-22.55}$	5.39
196973956	397635910581888512	3.19	0.04	34.94	3.74	3.14	1.68	0.21	$2.95^{+1.02}_{-0.23}$	$0.70^{+0.10}_{-0.19}$	$32.57^{+4.24}_{-4.89}$	$-6.49^{+8.59}_{-5.33}$	5.59
198152789	1505620405023410944	12.82	0.25	24.46	-15.35	-0.33	2.35	0.30	$12.84^{+0.69}_{-1.00}$	$0.45^{+0.26}_{-0.20}$	$25.44^{+3.98}_{-1.52}$	$-13.78^{+4.13}_{-7.85}$	3.48
458424681	4031670377528216320	31.98	0.49	33.42	-13.20	3.02	0.72	0.20	$31.98^{+0.02}_{-0.02}$	$0.34^{+0.08}_{-0.06}$	$13.12^{+2.22}_{-1.79}$	$-10.18^{+0.69}_{-0.66}$	1.22
46307919	611686051136877440	3.58	0.02	54.21	11.58	2.59	-0.14	0.35	$3.44^{+0.42}_{-0.55}$	$0.72^{+0.13}_{-0.18}$	$56.04^{+78.14}_{-8.62}$	$24.58^{+11.42}_{-13.47}$	5.94
429554271	3424894333005909504	1.02	0.29	26.15	8.38	1.47	2.55	0.09	$1.11^{+0.44}_{-0.68}$	$0.73^{+0.25}_{-0.25}$	$26.72^{+29.57}_{-4.81}$	$11.59^{+3.65}_{-2.76}$	7.25
26690153	1893702345536080256	2.36	0.21	53.30	-42.62	6.28	1.96	0.34	$2.34^{+0.79}_{-0.76}$	$0.73^{+0.08}_{-0.25}$	$58.33^{+4.96}_{-3.97}$	$-61.65^{+15.22}_{-8.72}$	6.75
20237221	1391723889583920768	4.32	0.07	23.89	-3.23	0.32	1.68	0.24	$4.50^{+0.65}_{-0.59}$	$0.50^{+0.17}_{-0.24}$	$31.91^{+17.03}_{-6.51}$	$-1.47^{+4.99}_{-6.25}$	6.06
20216313	1392056491851280640	212.34	0.76	22.05	-0.76	2.19	2.32	0.50	$212.35^{+0.10}_{-0.10}$	$0.79^{+0.04}_{-0.04}$	$21.89^{+2.20}_{-1.56}$	$-1.76^{+0.84}_{-0.78}$	1.00
219037973	1560561149934463104	171.56	0.32	17.42	-15.75	2.04	-0.98	0.61	$171.55^{+0.10}_{-0.10}$	$0.32^{+0.01}_{-0.01}$	$17.30^{+0.26}_{-0.26}$	$-15.75^{+0.16}_{-0.16}$	1.00
417546685	1384466288207118592	1.85	0.13	61.13	-32.11	-0.82	-1.54	0.28	$2.07^{+0.50}_{-0.46}$	$0.58^{+0.22}_{-0.28}$	$42.91^{+46.37}_{-8.41}$	$-23.30^{+13.15}_{-7.27}$	6.03
99252577	1009377860715543936	202.63	0.24	12.00	10.86	5.41	-0.04	0.48	$202.62^{+0.08}_{-0.08}$	$0.22^{+0.01}_{-0.01}$	$12.03^{+0.14}_{-0.14}$	$10.71^{+0.11}_{-0.11}$	1.00
81638394	3426751098906874624	37.21	0.03	10.14	16.68	0.97	0.41	0.22	$37.21^{+0.71}_{-0.93}$	$0.17^{+0.65}_{-0.15}$	$10.96^{+11.16}_{-1.03}$	$16.61^{+1.81}_{-2.11}$	1.83
...	...	...	...	...	...	...	...	...	...	...	...	...	...

Note—Columns 1-2 provide the identifiers for the target stars. Columns 4-9 list the orbital parameters for the binary systems, which were calculated using *The Joker*, along with the derived companion masses. The corresponding MCMC results are presented in columns 10-13. The final column shows the mean value of the MCMC Gelman–Rubin convergence statistic for all parameters. For detailed usage and caveats related to this table, please refer to Section 6. The complete table, which includes 297 stars, is available in its entirety in machine-readable format. A portion of the table is shown here to guide the reader regarding its form and content.

Table 8. Summary of RV Variable Catalog.

Sample	N_s	N_p	[Fe/H] (dex)	Exposure Number	ΔRV_{max}(km s^{-1})	T_{max} (hour)
Whole Multiple-epoch	113,792	114	$-0.095^{+0.19}_{-0.25}$	6^{+16}_{-3}	$5.19^{+6.16}_{-3.25}$	$1389.12^{+19531.28}_{-1388.33}$
RV Variable	41,382	37	$-0.106^{+0.18}_{-0.24}$	14^{+30}_{-8}	$10.16^{+16.17}_{-3.32}$	$10268.92^{+17136.52}_{-9883.97}$
Binary	7,846	6	$-0.054^{+0.20}_{-0.22}$	15^{+29}_{-9}	$46.16^{+201.06}_{-21.95}$	$17090.95^{+10858.65}_{-16130.93}$
RV Variable Without Binary	33,536	31	$-0.120^{+0.18}_{-0.25}$	14^{+30}_{-8}	$9.10^{+4.31}_{-2.55}$	$9863.13^{+17396.96}_{-9693.85}$
Short Time Scale	160	0	$-0.101^{+0.22}_{-0.27}$	3^{+0}_{-0}	$8.26^{+6.85}_{-2.83}$	$0.73^{+0.05}_{-0.28}$

4. ***ASAN-SN*** [15]: ASAS-SN (All-Sky Automated Survey for Supernovae) is the first optical survey to monitor the entire sky, with a cadence of about 24 hours down to $g\leq 18.5$ mag. As of 2024, ASAS-SN has discovered over 687,000 variable stars in the V-band (Shappee et al. 2014; Jayasinghe et al. 2021). We cross-matched the RV variable catalog with the ASAS-SN V-band catalog and identified 464 common sources. Among these, 343 were marked as variable stars in our catalog, including 222 eclipsing binaries, 71 spotted variables with rotational modulation, 16 δ Scuti-type variables (including 3 high-amplitude types), 4 young stellar objects, 3 RR Lyrae stars, 3 eruptive variables, and 24 variables with unspecified types.

   In addition, ASAS-SN provides a binary star database, which includes various physical parameters of binary systems derived from light curves (Rowan et al. 2023). They modeled the light curves of more than 30,000 detached eclipsing binaries from ASAS-SN and fitted the V- and g-band light curves, producing a catalog of orbital periods, eccentricities, and inclinations. Upon cross-matching this catalog with our RV variable catalog, we found 69 common sources, of which 57 were identified as binary stars in our catalog. Eleven of these were included in our well-fitted binary catalog, and the periods obtained from the RV curve fitting agreed with those from ASAS-SN.

5. ***TESS Eclipsing Binary Catalog*** [16]: The TESS Eclipsing Binary (EB) catalog provides a comprehensive list of eclipsing binary stars identified by the TESS mission (Prša et al. 2022). It includes detailed information on the eclipse depths, periods, and other properties of 4,584 systems. Using the TICs, we identified 36 matches between the TESS EB catalog and our RV variable catalog. Among these, 31 were labeled as binary stars in our catalog.

6. ***Gaia Non-Single Stars (NSS) Catalog*** [17]:The Gaia Non-Single Star (NSS) catalogs, released as part of Gaia DR3, provide a valuable resource for studying binary and multiple star systems by combining astrometric, spectroscopic, and photometric data from the Gaia mission (Gaia Collaboration et al. 2023b). These catalogs include orbital or trend solutions for approximately 800,000 systems covering various binary types. We cross-matched our RV-variable catalog with Gaia NSS sources classified under the eclipsing binary model, the single-lined spectroscopic binary (SB1) model, and the astrometric binary model. This yielded a total of 29 eclipsing binaries (EBs), 490 astrometric binaries, and 1,300 SB1s, with some sources appearing in multiple categories. Among these, 22 EBs, 102 astrometric binaries, and 711 SB1s are also labeled as binaries in our catalog.

In total, there are 4,901 common sources between our RV variable catalog and the referred variable catalogs such as VSX, Gaia DR3 variables, Gaia-NSS catalog, GCVS, and ASAS-SN variable catalogs. These include both extrinsic variables (e.g., binary systems), and intrinsic variables (e.g., pulsating and eruptive stars). None of the 297 well-fitted binary systems in our sample are identified as known variables of other types, among these, 192 are newly discovered binary star systems.

Among the matched sources with known binary classifications from referred catalogs, some systems are labeled as ‘RV variable’ in our catalog but not classified as ‘binary’. This discrepancy can be attributed to two main reasons. Taking the cross-match with the VSX catalog as an example, out of 108 such binaries, 64.8% (70 sources) exhibit RV amplitudes smaller than our threshold of 20 km s^{-1}, which we adopted to avoid potential contamination from spurious low-amplitude variability. Among the remaining 38 sources, the vast majority (35

[15] https://www.astronomy.ohio-state.edu/asassn/index.shtml
[16] https://tessebs.villanova.edu
[17] https://gea.esac.esa.int/archive/

sources out of 38) are very short-period binaries of periods less than 0.5 days. Due to the observing cadence and typical exposure intervals of the LAMOST survey, such short-period systems are inherently difficult to detect and accurately characterize in our catalog.

6. NOTABLE CAVEATS AND LIMITATIONS

Some of the caveats and assumptions of this study have been discussed in Section 3-5. These include the contamination of the binary catalog by intrinsic variable stars, and simplifications adopted when evaluating the selection criteria of binary candidates and deriving orbital parameters. During the RV curve fitting process, we found that RV measurements from certain LAMOST observing nights exhibit abnormally high or low values, likely due to instrumental or calibration issues. Moreover, incomplete RV phase coverage or poorly constrained RV fits may result in inaccurate orbital period estimates, such as overestimated values or periods that are integer multiples of the true value. Below, we summarize other key limitations and considerations:

1. Since our catalog includes stars with multiple observations, some of which are binary or variable stars, we incorporate different types of RV data. To accommodate the diversity of RV data, we introduced an 'RV Source Flag' for each star in our catalog (Column 38 in Table 2), indicating the type of RV measurement associated with each star: If the 'RV Source Flag' is set to 0, it indicates that the star does not have multiple epoch RV measurements, and its RV value corresponds to a single measurement from the LAMOST DR10 dataset. If the 'RV Source Flag' is set to 1, it indicates that the star has been identified as a binary system, and the RV value corresponds to the systemic velocity derived from fitting the binary star's radial velocity curve. If the 'RV Source Flag' is set to 2, it indicates that the star has multiple RV measurements, and the RV value is the average of those measurements. The RV data for stars with an 'RV Source Flag' of 2 should be used with caution, since they may exhibit RV variability across multiple epochs. Especially for those labeled as binaries ('Binary' flag = 1). This combination suggests that the RV difference exceeds 20 km s^{-1}, but the RV curve is poorly fitted, leading to an unreliable systemic velocity estimate.

2. While the kinematic ages with uncertainty $\sim 10\%$-20% were given for disk stars, the age-velocity dispersion relation is not suitable for halo and stream stars (as described in Chen et al. (2021b)). Moreover, the ages for each star calculated from J_Z using *zoomies* should only be used as a rough range, as the typical uncertainty is 3-4 Gyrs.

3. The use of LAMOST multiple RV observations to identify binary systems has certain limitations due to selection effects and observational constraints. The time span of the LAMOST MRS (less than 5 years) is not sufficient to effectively detect long-period binaries with orbital periods exceeding 50 years. Consequently, the binaries identified in this work are predominantly close binary systems, with a typical orbital period of ~10 days (See Section 5.4). In addition, LAMOST's typical exposure time of ~20 minutes and observation cadence pose challenges in detecting very short-period variables with rapidly varying RV.

4. For stars classified as 'RV variables' but not identified as 'binary' in Table 4, the observed RV variability may be attributed to long-period binary companions, intrinsic stellar variability (as discussed in Section 5.5), or photospheric activity. Stars classified as 'short time scale RV variables' may be compact object systems or binaries with very short orbital periods. For the identified binary systems, contamination from intrinsic variable stars cannot be fully excluded. To account for known variables identified in other catalogs, we include an additional flags in our catalog (Table 4).

5. For each of the binary candidates, we fitted their RV curve to derive orbital parameters (see Table 4). For the well-fitted systems, we also performed Markov Chain Monte Carlo (MCMC) sampling to obtain posterior distributions (see Table 7). However, we recommend using the orbital solutions returned by the sampling from *The Joker* software, as some of the MCMC results did not converge properly. Both sets of results are provided in Table 7, along with the Gelman-Rubin statistic to assess convergence.

6. During the RV curve fitting process, we found that some stars exhibit abnormally high or low RV values at specific observing epochs, deviating significantly (up to ~ 500 km s^{-1}) from the rest of their measurements, even in sources with more than 30 exposures. Upon further inspection, we noticed that many of these outlier measurements cluster around specific observing dates (e.g., MJD 58450, 58800, 59250), suggesting that they may be associated with instrumental or calibration issues during

certain LAMOST observing nights. To mitigate the impact of such issues, we applied additional filtering stpdf. In particular, we removed exposures from nights with only a single observation when constructing our multi-epoch sample, and we excluded sources affected by these outliers during the selection of the well-fitted sample. Nonetheless, we acknowledge that some residual contamination may still remain. We therefore commend users of the LAMOST time-domain RV data, especially those analyzing individual sources, to be aware of possible instrumental artifacts and consider them as a potential source of contamination when doing a large sample analysis.

7. SUMMARY

In this work, we constructed kinematic-chemical catalogs (Table 2 and a similar table for the LRS sample) by combining TESS, Gaia DR3, and LAMOST DR10 data (Section 2), we also identified RV variables in the sample and characterized kinematic and orbital properties of the identified binary candidates (Table 4 and 7). Detailed caveats and recommended guidelines for using the released catalogs are provided in Section 6. The kinematic catalogs include 207,690 stars with MRS spectral data and 452,803 stars with LRS spectral data (Section 4, Table 2). Using LAMOST spectroscopic and Gaia astrometric data, we calculated each star's space position and Galactic orbit parameters (i.e., velocity, angular momentum, actions; Section 3.1). Applying the revised kinematic methods from PAST I (Chen et al. 2021b), we derived the Galactic component membership probabilities and then classified stars into different components (Section 3.2). Additionally, we obtained the ages for individual stars based on vertical actions J_Z using the *zoomies* package, though the typical uncertainty is relatively large (60%-80%). Alternatively, the average kinematic age for a group of stars can be derived from velocity dispersion, with a much smaller typical uncertainty of 10% – 20% by adopting the revised AVR from the PAST series (Section 3.3).

Based on our constructed LAMOST-Gaia-TESS catalogs, we further investigated the kinematics and chemical abundances of different Galactic components (Table 3). As expected, from the thin disk, thick disk to the halo, Galactic velocities and radial orbital action (J_R) increase, while vertical angular momentum (L_Z) decreases (Figure 3-4). Additionally, stellar ages grow older, [Fe/H] decreases, and [α/Fe] increases (Figures 5–6). By adopting the kinematic planes from Kushniruk & Bensby (2019), we also identified stars associated with 12 nearby streams (Figure 7), and found that stars within a given stream exhibit very similar kinematic and chemical properties. Our results show that most TESS-detected planets are hot Jupiters orbiting thin disk stars, while no hot planets (period < 10 days) are detected around thick disk stars (Figure 8).

Using multiple-epoch RV measurements from LAMOST, we identified 41,445 RV variables in our LAMOST-Gaia-TESS sample based on the selection criteria in Equations 2 and 3 (Section 5.2, Table 4). Among them, 7,846 were classified as high-confidence binary candidates since they exhibit significant RV variations and have peak-to-peak RV variation exceeding 20 km s^{-1}. To evaluate the effectiveness of our selection method, we conducted a Monte Carlo simulation to assess the impact of the adopted parameters on purity, detection rate, and completeness of the binary star identification (Table 5, Figure 10).

For these binary candidates, we further derived orbital parameters by fitting their RV curves using *The Joker*. Combing the fitted systemic velocities with astrometry data, we also determined their kinematic properties (see columns in Table 4). After inspecting the RV curves, we obtained a sample of 297 binaries with well-constrained orbital solutions (Table 7). We found the sample is dominated by close binaries with orbital periods < 10 days and the mass ratio distributions peaking between 0.3 and 0.5 (Figure 12). We also observed a significantly positive correlation between orbital period and eccentricity, indicating the effects of tidal circularization (Section 5.4). The combination of orbital and kinematic parameters from our well-fitted binary catalog provides a data basis for exploring how these correlations vary with kinematic age and other stellar properties, such as effective temperature and mass ratio, which will be addressed in future work.

The LAMOST-Gaia-TESS kinematic catalog constructed in this work is useful for future research on exoplanets in different Galactic environments (e.g., position, components, age, history, and chemistry). Additionally, applying our RV variable identification method to future LAMOST releases will yield more binaries, including planet-hosting stars. With the characterized kinematics and orbital properties, the RV variable and binary sample we identified will facilitate statistical analyses of the evolution and interactions of close binaries, as well as their impact on planetary systems. Together, these studies based on our catalogs will deepen the understanding of stellar and planetary formation and evolution within the context of the Milky Way.

ACKNOWLEDGMENTS

This work is supported by the National Key R&D Program of China (2024YFA1611803) and the National Natural Science Foundation of China (NSFC; grant No. 12273011, 12150009, 12403071). We also acknowledge the science research grants from the China Manned Space Project with NO.CMS-CSST-2021-B12. J.-W.X. also acknowledges the support from the National Youth Talent Support Program. H.F.W. is supported by the Department of Physics and Astronomy of Padova University through the 2022 ARPE grant: Rediscovering our Galaxy with Machines. W.Z. acknowledges the support from the Central Guidance for Local Science and Technology Development Fund, No. ZYYD2025QY27. S.D. is supported by the National Natural Science Foundation of China (Grant No. 12133005) and the China Manned Space Program with grant no. CMS-CSST-2025-A16. S.D. acknowledges the New Cornerstone Science Foundation through the XPLORER PRIZE.

This paper includes data collected by the TESS mission. Funding for the TESS mission is provided by the NASA's Science Mission Directorate. This work has included data from Guoshoujing Telescope (the Large Sky AreaMulti-Object Fiber Spectroscopic Telescope LAMOST), which is a National Major Scientific Project built by the Chinese Academy of Sciences. Funding for the project has been provided by the National Development and Reform Commission. LAMOST is operated and managed by the National Astronomical Observatories, Chinese Academy of Sciences. This work has made use of data from the European Space Agency (ESA) mission *Gaia* (https://www.cosmos.esa.int/gaia), processed by the *Gaia* Data Processing and Analysis Consortium (DPAC, https://www.cosmos.esa.int/web/gaia/dpac/consortium). Funding for the DPAC has been provided by national institutions, in particular the institutions participating in the *Gaia* Multilateral Agreement.

REFERENCES

Abril-Pla, O., Andreani, V., Carroll, C., et al. 2023, PeerJ Computer Science, 9, e1516, doi: 10.7717/peerj-cs.1516

Anderson, R. I., Viviani, G., Shetye, S. S., et al. 2024, A&A, 686, A177, doi: 10.1051/0004-6361/202348400

Badenes, C., & Maoz, D. 2012, ApJL, 749, L11, doi: 10.1088/2041-8205/749/1/L11

Badenes, C., Mazzola, C., Thompson, T. A., et al. 2018, ApJ, 854, 147, doi: 10.3847/1538-4357/aaa765

Baglin, A., Auvergne, M., Boisnard, L., et al. 2006, in 36th COSPAR Scientific Assembly, Vol. 36, 3749

Barker, A. J. 2022, ApJL, 927, L36, doi: 10.3847/2041-8213/ac5b63

Bashi, D., & Belokurov, V. 2025, MNRAS, 541, 2008, doi: 10.1093/mnras/staf1102

Bashi, D., Belokurov, V., & Hodgkin, S. 2024, MNRAS, 535, 949, doi: 10.1093/mnras/stae2385

Bashi, D., Mazeh, T., & Faigler, S. 2023, MNRAS, 522, 1184, doi: 10.1093/mnras/stad999

Bashi, D., Shahaf, S., Mazeh, T., et al. 2022, MNRAS, 517, 3888, doi: 10.1093/mnras/stac2928

Bashi, D., & Tokovinin, A. 2024, A&A, 692, A247, doi: 10.1051/0004-6361/202452637

Bashi, D., & Zucker, S. 2019, AJ, 158, 61, doi: 10.3847/1538-3881/ab27c9

—. 2022, MNRAS, 510, 3449, doi: 10.1093/mnras/stab3596

Beaton, R. L., Bono, G., Braga, V. F., et al. 2018, SSRv, 214, 113, doi: 10.1007/s11214-018-0542-1

Beleznay, M., & Kunimoto, M. 2022, MNRAS, 516, 75, doi: 10.1093/mnras/stac2179

Belokurov, V., Sanders, J. L., Fattahi, A., et al. 2020, MNRAS, 494, 3880, doi: 10.1093/mnras/staa876

Bensby, T., Feltzing, S., & Lundström, I. 2003, Astronomy & Astrophysics, 410, 527, doi: 10.1051/0004-6361:20031213

Bensby, T., Feltzing, S., & Oey, M. S. 2014, Astronomy & Astrophysics, 562, A71, doi: 10.1051/0004-6361/201322631

Bonaca, A., Conroy, C., Wetzel, A., Hopkins, P. F., & Kereš, D. 2017, ApJ, 845, 101, doi: 10.3847/1538-4357/aa7d0c

Bonaca, A., & Price-Whelan, A. M. 2025, NewAR, 100, 101713, doi: 10.1016/j.newar.2024.101713

Bonidie, V., Court, T., Daher, C. M., et al. 2022, ApJL, 933, L18, doi: 10.3847/2041-8213/ac79af

Bono, G., Braga, V. F., Crestani, J., et al. 2020, ApJL, 896, L15, doi: 10.3847/2041-8213/ab9538

Borucki, W. J. 2016, Reports on Progress in Physics, 79, 036901, doi: 10.1088/0034-4885/79/3/036901

Borucki, W. J., Koch, D., Basri, G., et al. 2010, Science, 327, 977, doi: 10.1126/science.1185402

Bryant, E. M., Bayliss, D., & Van Eylen, V. 2023, MNRAS, 521, 3663, doi: 10.1093/mnras/stad626

Cantat-Gaudin, T., Jordi, C., Vallenari, A., et al. 2018, A&A, 618, A93, doi: 10.1051/0004-6361/201833476

Carmichael, T. W. 2023, MNRAS, 519, 5177, doi: 10.1093/mnras/stac3720

Carney, B. W., Latham, D. W., Stefanik, R. P., Laird, J. B., & Morse, J. A. 2003, AJ, 125, 293, doi: 10.1086/345386

Carrillo, A., Hawkins, K., Bowler, B. P., Cochran, W., & Vanderburg, A. 2020, MNRAS, 491, 4365, doi: 10.1093/mnras/stz3255

Chen, D.-C., Xie, J.-W., Zhou, J.-L., et al. 2025, Nature Astronomy, doi: 10.1038/s41550-025-02693-6

Chen, D.-C., Yang, J.-Y., Xie, J.-W., et al. 2021a, The Astronomical Journal, 162, 100, doi: 10.3847/1538-3881/ac0f08

Chen, D.-C., Xie, J.-W., Zhou, J.-L., et al. 2021b, The Astrophysical Journal, 909, 115, doi: 10.3847/1538-4357/abd5be

Chen, D.-C., Xie, J.-W., Zhou, J.-L., et al. 2022, AJ, 163, 249, doi: 10.3847/1538-3881/ac641f

—. 2023, Proceedings of the National Academy of Science, 120, e2304179120, doi: 10.1073/pnas.2304179120

Chen, D.-C., Xie, J.-W., Zhou, J.-L., et al. 2023, Proceedings of the National Academy of Science, 120, e2304179120, doi: 10.1073/pnas.2304179120

Chen, X., Liu, Z., & Han, Z. 2024, Progress in Particle and Nuclear Physics, 134, 104083, doi: 10.1016/j.ppnp.2023.104083

Chen, Y., Xia, F., Wang, X., Fu, Y., & Yuan, Y. 2023, ApJS, 269, 41, doi: 10.3847/1538-4365/acfcb3

Clementini, G., Ripepi, V., Garofalo, A., et al. 2023, A&A, 674, A18, doi: 10.1051/0004-6361/202243964

Conroy, C., & Wechsler, R. H. 2009, ApJ, 696, 620, doi: 10.1088/0004-637X/696/1/620

Cui, X.-Q., Zhao, Y.-H., Chu, Y.-Q., et al. 2012, Research in Astronomy and Astrophysics, 12, 1197, doi: 10.1088/1674-4527/12/9/003

Daher, C. M., Badenes, C., Tayar, J., et al. 2022, MNRAS, 512, 2051, doi: 10.1093/mnras/stac590

Dai, Y.-Z., Liu, H.-G., Yang, J.-Y., & Zhou, J.-L. 2023, AJ, 166, 219, doi: 10.3847/1538-3881/acff67

Darragh-Ford, E., Hunt, J. A. S., Price-Whelan, A. M., & Johnston, K. V. 2023, ApJ, 955, 74, doi: 10.3847/1538-4357/acf1fc

Dong, S., Katz, B., & Socrates, A. 2014, ApJL, 781, L5, doi: 10.1088/2041-8205/781/1/L5

Duchêne, G., & Kraus, A. 2013, Annual Review of Astronomy and Astrophysics, 51, 269, doi: 10.1146/annurev-astro-081710-102602

Dunstall, P. R., Dufton, P. L., Sana, H., et al. 2015, Astronomy and Astrophysics, 580, A93, doi: 10.1051/0004-6361/201526192

Eilers, A.-C., Hogg, D. W., Rix, H.-W., & Ness, M. K. 2019, ApJ, 871, 120, doi: 10.3847/1538-4357/aaf648

El-Badry, K., & Rix, H.-W. 2019, MNRAS, 482, L139, doi: 10.1093/mnrasl/sly206

El-Badry, K., Rix, H.-W., & Heintz, T. M. 2021, MNRAS, 506, 2269, doi: 10.1093/mnras/stab323

El-Badry, K., Ting, Y.-S., Rix, H.-W., et al. 2018, MNRAS, 476, 528, doi: 10.1093/mnras/sty240

Eyer, L., Audard, M., Holl, B., et al. 2023, Astronomy & Astrophysics, 674, A13, doi: 10.1051/0004-6361/202244242

Faber, J. A., Rasio, F. A., & Willems, B. 2005, Icarus, 175, 248, doi: 10.1016/j.icarus.2004.10.021

Feinstein, A. D., Seligman, D. Z., Günther, M. N., & Adams, F. C. 2022, ApJL, 925, L9, doi: 10.3847/2041-8213/ac4b5e

Fernández-Alvar, E., Fernández-Trincado, J. G., Moreno, E., et al. 2019, MNRAS, 487, 1462, doi: 10.1093/mnras/stz1299

Fouesneau, M., Frémat, Y., Andrae, R., et al. 2023, Astronomy & Astrophysics, 674, A28, doi: 10.1051/0004-6361/202243919

Gaia Collaboration, Vallenari, A., Brown, A. G. A., et al. 2023a, Astronomy & Astrophysics, 674, A1, doi: 10.1051/0004-6361/202243940

Gaia Collaboration, Arenou, F., Babusiaux, C., et al. 2023b, A&A, 674, A34, doi: 10.1051/0004-6361/202243782

Gan, T., Theissen, C. A., Wang, S. X., Burgasser, A. J., & Mao, S. 2025, ApJS, 276, 47, doi: 10.3847/1538-4365/ad9c65

Gan, T., Wang, S. X., Wang, S., et al. 2023, AJ, 165, 17, doi: 10.3847/1538-3881/ac9b12

Gao, S., Liu, C., Zhang, X., et al. 2014, ApJL, 788, L37, doi: 10.1088/2041-8205/788/2/L37

Gao, S., Zhao, H., Yang, H., & Gao, R. 2017, Monthly Notices of the Royal Astronomical Society: Letters, 469, L68, doi: 10.1093/mnrasl/slx048

Gao, S., Zhao, H., Yang, H., & Gao, R. 2017, MNRAS, 469, L68, doi: 10.1093/mnrasl/slx048

Geller, A. M., & Mathieu, R. D. 2012, AJ, 144, 54, doi: 10.1088/0004-6256/144/2/54

Geller, A. M., Mathieu, R. D., Latham, D. W., et al. 2021, AJ, 161, 190, doi: 10.3847/1538-3881/abdd23

Gelman, A., & Rubin, D. B. 1992, Statistical Science, 7, 457, doi: 10.1214/ss/1177011136

Giesers, B., Kamann, S., Dreizler, S., et al. 2019, A&A, 632, A3, doi: 10.1051/0004-6361/201936203

Guerrero, N. M., Seager, S., Huang, C. X., et al. 2021, The Astrophysical Journal Supplement Series, 254, 39, doi: 10.3847/1538-4365/abefe1

Günther, M. N., Pozuelos, F. J., Dittmann, J. A., et al. 2019, Nature Astronomy, 3, 1099, doi: 10.1038/s41550-019-0845-5

Guo, S., Kovalev, M., Li, J., et al. 2025, ApJS, 278, 46, doi: 10.3847/1538-4365/adced1

Guo, X., Johnson, J. A., Mann, A. W., et al. 2017, ApJ, 838, 25, doi: 10.3847/1538-4357/aa6004

Guo, Y., Liu, C., Wang, L., et al. 2022, A&A, 667, A44, doi: 10.1051/0004-6361/202244300

Guo, Y., Li, J., Xiong, J., et al. 2022, Research in Astronomy and Astrophysics, 22, 025009, doi: 10.1088/1674-4527/ac3e5a

Hamer, J. H., & Schlaufman, K. C. 2019, AJ, 158, 190, doi: 10.3847/1538-3881/ab3c56

—. 2024, AJ, 167, 55, doi: 10.3847/1538-3881/ad110e

Han, X., Wang, H.-F., Carraro, G., et al. 2025, The Astrophysical Journal, 985, 32, doi: 10.3847/1538-4357/adc4e5

Hansen, T. T., Andersen, J., Nordström, B., et al. 2016a, A&A, 586, A160, doi: 10.1051/0004-6361/201527235

—. 2016b, A&A, 588, A3, doi: 10.1051/0004-6361/201527409

Hasanzadeh, A., Safari, H., & Ghasemi, H. 2021, MNRAS, 505, 1476, doi: 10.1093/mnras/stab1411

Holman, M. J., & Wiegert, P. A. 1999, AJ, 117, 621, doi: 10.1086/300695

Hon, M., Huber, D., Kuszlewicz, J. S., et al. 2021, ApJ, 919, 131, doi: 10.3847/1538-4357/ac14b1

Huang, C. X., Burt, J., Vanderburg, A., et al. 2018, ApJL, 868, L39, doi: 10.3847/2041-8213/aaef91

IJspeert, L. W., Tkachenko, A., Johnston, C., & Aerts, C. 2024, A&A, 691, A242, doi: 10.1051/0004-6361/202450507

Jackson, B., Barnes, R., & Greenberg, R. 2009, ApJ, 698, 1357, doi: 10.1088/0004-637X/698/2/1357

Jayasinghe, T., Kochanek, C. S., Stanek, K. Z., et al. 2021, Monthly Notices of the Royal Astronomical Society, 503, 200, doi: 10.1093/mnras/stab114

Joergens, V., Müller, A., & Reffert, S. 2010, A&A, 521, A24, doi: 10.1051/0004-6361/201014853

Johnson, D. R. H., & Soderblom, D. R. 1987, The Astronomical Journal, 93, 864, doi: 10.1086/114370

Johnson, J. A., Aller, K. M., Howard, A. W., & Crepp, J. R. 2010, PASP, 122, 905, doi: 10.1086/655775

Justesen, A. B., & Albrecht, S. 2021, ApJ, 912, 123, doi: 10.3847/1538-4357/abefcd

Kanodia, S., Cañas, C. I., Mahadevan, S., et al. 2024, AJ, 167, 161, doi: 10.3847/1538-3881/ad27cb

Katz, B., Dong, S., & Malhotra, R. 2011, PhRvL, 107, 181101, doi: 10.1103/PhysRevLett.107.181101

Katz, D., Sartoretti, P., Guerrier, A., et al. 2023, Astronomy & Astrophysics, 674, A5, doi: 10.1051/0004-6361/202244220

Khaliullin, K. F., & Khaliullina, A. I. 2011, MNRAS, 411, 2804, doi: 10.1111/j.1365-2966.2010.17878.x

Knutson, H. A., Fulton, B. J., Montet, B. T., et al. 2014, ApJ, 785, 126, doi: 10.1088/0004-637X/785/2/126

Kounkel, M., Covey, K. R., Stassun, K. G., et al. 2021, AJ, 162, 184, doi: 10.3847/1538-3881/ac1798

Kraus, A. L., Ireland, M. J., Huber, D., Mann, A. W., & Dupuy, T. J. 2016, AJ, 152, 8, doi: 10.3847/0004-6256/152/1/8

Kushniruk, I., & Bensby, T. 2019, A&A, 631, A47, doi: 10.1051/0004-6361/201935234

Kushniruk, I., Bensby, T., Feltzing, S., et al. 2020, A&A, 638, A154, doi: 10.1051/0004-6361/202037923

Latham, D. W., Stefanik, R. P., Torres, G., et al. 2002, AJ, 124, 1144, doi: 10.1086/341384

Lee, Y. S., Beers, T. C., An, D., et al. 2011, The Astrophysical Journal, 738, 187, doi: 10.1088/0004-637X/738/2/187

Leiner, E. M., Mathieu, R. D., Gosnell, N. M., & Geller, A. M. 2015, AJ, 150, 10, doi: 10.1088/0004-6256/150/1/10

Levrard, B., Winisdoerffer, C., & Chabrier, G. 2009, ApJL, 692, L9, doi: 10.1088/0004-637X/692/1/L9

Li, C., de Grijs, R., Deng, L., et al. 2016, Nature, 529, 502, doi: 10.1038/nature16493

Li, J., Li, J.-D., Guo, Y.-J., et al. 2023, Chinese Physics B, 32, 019501, doi: 10.1088/1674-1056/ac9362

Lindegren, L., Klioner, S. A., Hernández, J., et al. 2021, Astronomy & Astrophysics, 649, A2, doi: 10.1051/0004-6361/202039709

Lithwick, Y., & Naoz, S. 2011, ApJ, 742, 94, doi: 10.1088/0004-637X/742/2/94

Liu, C., Fu, J., Shi, J., et al. 2020, LAMOST Medium-Resolution Spectroscopic Survey (LAMOST-MRS): Scientific Goals and Survey Plan, arXiv. https://arxiv.org/abs/2005.07210

Liu, H.-B., Gu, W.-M., Zhang, Z.-X., et al. 2024, The Astrophysical Journal, 969, 114, doi: 10.3847/1538-4357/ad4c6f

Luo, A.-L., Zhao, Y.-H., Zhao, G., et al. 2015, Research in Astronomy and Astrophysics, 15, 1095, doi: 10.1088/1674-4527/15/8/002

Luo, F., Zhao, Y.-H., Li, J., Guo, Y.-J., & Liu, C. 2021, Research in Astronomy and Astrophysics, 21, 272, doi: 10.1088/1674-4527/21/11/272

Lustig-Yaeger, J., Fu, G., May, E. M., et al. 2023, Nature Astronomy, 7, 1317, doi: 10.1038/s41550-023-02064-z

Mahy, L., Lanthermann, C., Hutsemékers, D., et al. 2022, A&A, 657, A4, doi: 10.1051/0004-6361/202040062

Maoz, D., Badenes, C., & Bickerton, S. J. 2012, ApJ, 751, 143, doi: 10.1088/0004-637X/751/2/143

Mateu, C., & Vivas, A. K. 2018, MNRAS, 479, 211, doi: 10.1093/mnras/sty1373

Mayor, M., & Queloz, D. 1995, Nature, 378, 355, doi: 10.1038/378355a0

Mazeh, T. 2008, in EAS Publications Series, Vol. 29, EAS Publications Series, ed. M. J. Goupil & J. P. Zahn (EDP), 1–65, doi: 10.1051/eas:0829001

Mazzola, C. N., Badenes, C., Moe, M., et al. 2020, MNRAS, 499, 1607, doi: 10.1093/mnras/staa2859

McTier, M. A. S., & Kipping, D. M. 2019, MNRAS, 489, 2505, doi: 10.1093/mnras/stz2088

Meibom, S., & Mathieu, R. D. 2005, The Astrophysical Journal, 620, 970, doi: 10.1086/427082

Meibom, S., Mathieu, R. D., & Stassun, K. G. 2006, ApJ, 653, 621, doi: 10.1086/508252

Milliman, K. E., Mathieu, R. D., Geller, A. M., et al. 2014, AJ, 148, 38, doi: 10.1088/0004-6256/148/2/38

Moe, M., & Di Stefano, R. 2017, The Astrophysical Journal Supplement Series, 230, 15, doi: 10.3847/1538-4365/aa6fb6

Moe, M., Kratter, K. M., & Badenes, C. 2019, ApJ, 875, 61, doi: 10.3847/1538-4357/ab0d88

Navarro, J. F., Frenk, C. S., & White, S. D. M. 1996, ApJ, 462, 563, doi: 10.1086/177173

Ngo, H., Knutson, H. A., Hinkley, S., et al. 2015, ApJ, 800, 138, doi: 10.1088/0004-637X/800/2/138

—. 2016, ApJ, 827, 8, doi: 10.3847/0004-637X/827/1/8

Nine, A. C., Milliman, K. E., Mathieu, R. D., et al. 2020, AJ, 160, 169, doi: 10.3847/1538-3881/abad3b

Offner, S. S. R., Moe, M., Kratter, K. M., et al. 2023, in Astronomical Society of the Pacific Conference Series, Vol. 534, Protostars and Planets VII, ed. S. Inutsuka, Y. Aikawa, T. Muto, K. Tomida, & M. Tamura, 275, doi: 10.48550/arXiv.2203.10066

Ogilvie, G. I., & Lin, D. N. C. 2007, ApJ, 661, 1180, doi: 10.1086/515435

Paegert, M., Stassun, K. G., Collins, K. A., et al. 2021, arXiv e-prints, arXiv:2108.04778, doi: 10.48550/arXiv.2108.04778

Percy, J. R. 2007, Understanding Variable Stars (Cambridge University Press), doi: 10.1017/CBO9780511536489

Petrovich, C. 2015a, ApJ, 799, 27, doi: 10.1088/0004-637X/799/1/27

—. 2015b, ApJ, 805, 75, doi: 10.1088/0004-637X/805/1/75

Plachy, E., Pál, A., Bódi, A., et al. 2021, ApJS, 253, 11, doi: 10.3847/1538-4365/abd4e3

Posti, L., Helmi, A., Veljanoski, J., & Breddels, M. A. 2018, A&A, 615, A70, doi: 10.1051/0004-6361/201732277

Pourbaix, D., Tokovinin, A. A., Batten, A. H., et al. 2004, A&A, 424, 727, doi: 10.1051/0004-6361:20041213

Price-Whelan, A. M. 2017, The Journal of Open Source Software, 2, 388, doi: 10.21105/joss.00388

Price-Whelan, A. M., Hogg, D. W., Foreman-Mackey, D., & Rix, H.-W. 2017, The Astrophysical Journal, 837, 20, doi: 10.3847/1538-4357/aa5e50

Price-Whelan, A. M., Hogg, D. W., Rix, H.-W., et al. 2018, The Astronomical Journal, 156, 18, doi: 10.3847/1538-3881/aac387

—. 2020, The Astrophysical Journal, 895, 2, doi: 10.3847/1538-4357/ab8acc

Prša, A., Batalha, N., Slawson, R. W., et al. 2011, The Astronomical Journal, 141, 83, doi: 10.1088/0004-6256/141/3/83

Prša, A., Kochoska, A., Conroy, K. E., et al. 2022, The Astrophysical Journal Supplement Series, 258, 16, doi: 10.3847/1538-4365/ac324a

Raghavan, D., McAlister, H. A., Henry, T. J., et al. 2010, The Astrophysical Journal Supplement Series, 190, 1, doi: 10.1088/0067-0049/190/1/1

Recio-Blanco, A., de Laverny, P., Palicio, P. A., et al. 2023, A&A, 674, A29, doi: 10.1051/0004-6361/202243750

Ricker, G. R., Winn, J. N., Vanderspek, R., et al. 2015, Journal of Astronomical Telescopes, Instruments, and Systems, 1, 014003, doi: 10.1117/1.JATIS.1.1.014003

Riello, M., De Angeli, F., Evans, D. W., et al. 2021, A&A, 649, A3, doi: 10.1051/0004-6361/202039587

Ripepi, V., Clementini, G., Molinaro, R., et al. 2023, A&A, 674, A17, doi: 10.1051/0004-6361/202243990

Ritchie, B. W., Clark, J. S., Negueruela, I., & Crowther, P. A. 2009, A&A, 507, 1585, doi: 10.1051/0004-6361/200912686

Rosenthal, L. J., Fulton, B. J., Hirsch, L. A., et al. 2021, ApJS, 255, 8, doi: 10.3847/1538-4365/abe23c

Rowan, D. M., Jayasinghe, T., Stanek, K. Z., et al. 2023, Monthly Notices of the Royal Astronomical Society, 523, 2641, doi: 10.1093/mnras/stad1560

Sagear, S., Price-Whelan, A. M., Ballard, S., et al. 2024, ApJ, 977, 49, doi: 10.3847/1538-4357/ad8b26

Samus', N. N., Kazarovets, E. V., Durlevich, O. V., Kireeva, N. N., & Pastukhova, E. N. 2017, Astronomy Reports, 61, 80, doi: 10.1134/S1063772917010085

Sana, H., De Mink, S. E., De Koter, A., et al. 2012, Science, 337, 444, doi: 10.1126/science.1223344

Sana, H., de Koter, A., de Mink, S. E., et al. 2013, Astronomy & Astrophysics, 550, A107, doi: 10.1051/0004-6361/201219621

Shappee, B. J., Prieto, J. L., Grupe, D., et al. 2014, The Astrophysical Journal, 788, 48, doi: 10.1088/0004-637X/788/1/48

Stassun, K. G., Oelkers, R. J., Pepper, J., et al. 2018, The Astronomical Journal, 156, 102, doi: 10.3847/1538-3881/aad050

Stassun, K. G., Oelkers, R. J., Paegert, M., et al. 2019, The Astronomical Journal, 158, 138, doi: 10.3847/1538-3881/ab3467

Szabó, Z. M., Kóspál, Á., Ábrahám, P., et al. 2021, ApJ, 917, 80, doi: 10.3847/1538-4357/ac04b3

The GRAVITY Collaboration, Abuter, R., Amorim, A., et al. 2019, Astronomy & Astrophysics, 625, L10, doi: 10.1051/0004-6361/201935656

Tian, H.-J., Liu, C., Carlin, J. L., et al. 2015, The Astrophysical Journal, 809, 145, doi: 10.1088/0004-637X/809/2/145

Tian, Z., Liu, X., Yuan, H., et al. 2020, The Astrophysical Journal Supplement Series, 249, 22, doi: 10.3847/1538-4365/ab9904

Tian, Z.-J., Liu, X.-W., Yuan, H.-B., et al. 2018, Research in Astronomy and Astrophysics, 18, 052, doi: 10.1088/1674-4527/18/5/52

Traven, G., Feltzing, S., Merle, T., et al. 2020, A&A, 638, A145, doi: 10.1051/0004-6361/202037484

Triaud, A. H. M. J., Martin, D. V., Ségransan, D., et al. 2017, A&A, 608, A129, doi: 10.1051/0004-6361/201730993

Tu, P.-W., Xie, J.-W., Chen, D.-C., & Zhou, J.-L. 2025, Nature Astronomy, 9, 995, doi: 10.1038/s41550-025-02539-1

Tu, Z.-L., Yang, M., Wang, H. F., & Wang, F. Y. 2021, ApJS, 253, 35, doi: 10.3847/1538-4365/abda3c

Van Eylen, V., Winn, J. N., & Albrecht, S. 2016, ApJ, 824, 15, doi: 10.3847/0004-637X/824/1/15

Wang, J., Fischer, D. A., Xie, J.-W., & Ciardi, D. R. 2015, ApJ, 813, 130, doi: 10.1088/0004-637X/813/2/130

Wang, J., Shi, J., Fu, J., Zong, W., & Li, C. 2024, ApJS, 272, 31, doi: 10.3847/1538-4365/ad43d5

Wang, J., Xie, J.-W., Barclay, T., & Fischer, D. A. 2014, ApJ, 783, 4, doi: 10.1088/0004-637X/783/1/4

Watson, C. L., Henden, A. A., & Price, A. 2006, Society for Astronomical Sciences Annual Symposium, 25, 47

Weldon, G. C., Naoz, S., & Hansen, B. M. S. 2025, ApJL, 980, L31, doi: 10.3847/2041-8213/adb157

Windemuth, D., Agol, E., Ali, A., & Kiefer, F. 2019, MNRAS, 489, 1644, doi: 10.1093/mnras/stz2137

Winn, J. N. 2024, The Transiting Exoplanet Survey Satellite, arXiv. https://arxiv.org/abs/2410.12905

Winn, J. N., & Fabrycky, D. C. 2015, ARA&A, 53, 409, doi: 10.1146/annurev-astro-082214-122246

Winter, A. J., Kruijssen, J. M. D., Longmore, S. N., & Chevance, M. 2020, Nature, 586, 528, doi: 10.1038/s41586-020-2800-0

Wu, Y., Du, B., Luo, A., Zhao, Y., & Yuan, H. 2014, in IAU Symposium, Vol. 306, Statistical Challenges in 21st Century Cosmology, ed. A. Heavens, J.-L. Starck, & A. Krone-Martins, 340–342, doi: 10.1017/S1743921314010825

Xiang, M. S., Liu, X. W., Yuan, H. B., et al. 2015, Monthly Notices of the Royal Astronomical Society, 448, 822, doi: 10.1093/mnras/stu2692

Xing, K., Zong, W., Silvotti, R., et al. 2024, ApJS, 271, 57, doi: 10.3847/1538-4365/ad2ddd

Yan, H., Li, H., Wang, S., et al. 2022, The Innovation, 3, 100224, doi: 10.1016/j.xinn.2022.100224

Yan, Y., Du, C., Li, H., et al. 2020, ApJ, 903, 131, doi: 10.3847/1538-4357/abbd3d

Yang, J.-Y., Chen, D.-C., Xie, J.-W., et al. 2023, The Astronomical Journal, 166, 243, doi: 10.3847/1538-3881/ad0368

Zahn, J. P. 1975, A&A, 41, 329

—. 1989, A&A, 220, 112

Zahn, J.-P. 2008, EAS Publications Series, 29, 67, doi: 10.1051/eas:0829002

Zahn, J. P., & Bouchet, L. 1989, A&A, 223, 112

Zanazzi, J. J. 2022, ApJL, 929, L27, doi: 10.3847/2041-8213/ac6516

Zhang, M., Hu, R., Inglis, J., et al. 2024, ApJL, 961, L44, doi: 10.3847/2041-8213/ad1a07

Zhao, G., Zhao, Y.-H., Chu, Y.-Q., Jing, Y.-P., & Deng, L.-C. 2012, Research in Astronomy and Astrophysics, 12, 723, doi: 10.1088/1674-4527/12/7/002

Zhu, H., Du, C., Yan, Y., et al. 2021, ApJ, 915, 9, doi: 10.3847/1538-4357/abff52

Zhu, W., & Dong, S. 2021, ARA&A, 59, 291, doi: 10.1146/annurev-astro-112420-020055

Zink, J. K., Hardegree-Ullman, K. K., Christiansen, J. L., et al. 2023, AJ, 165, 262, doi: 10.3847/1538-3881/acd24c

Zong, W., Fu, J.-N., Cat, P. D., et al. 2020, The Astrophysical Journal Supplement Series, 251, 15, doi: 10.3847/1538-4365/abbb2d

APPENDIX

A. RESULTS FOR LRS

The kinematic and chemical properties of the LRS sample, in the same format as Table 3, are presented here (Table A1). Corresponding figures for the LRS sample are also shown (Figure A1-A6), analogous to Figures 2–7 for the MRS sample.

Table A1. Kinematic and chemical properties of different Galactic components for the LAMOST_LRS-Gaia-TESS sample.

Components	N_s	N_p	V_{tot}	[Fe/H]	[α/Fe]	L_Z	$\sqrt{J_R}$	$\ln(J_Z)$	Age_{kin}	$Age_{zoomies}$
					LRS					
Thin disk	372,923	270	$35.4^{+22.1}_{-15.6}$	$-0.06^{+0.20}_{-0.24}$	$0.06^{+0.11}_{-0.12}$	1889^{+180}_{-239}	$4.6^{+3.2}_{-2.4}$	$1.3^{+1.1}_{-1.5}$	$2.52^{+0.31}_{-0.24}$	$1.18^{+1.86}_{-1.18}$
Thick disk	19,215	5	$100.1^{+31.0}_{-19.2}$	$-0.36^{+0.36}_{-0.29}$	$0.19^{+0.17}_{-0.19}$	1389^{+375}_{-212}	$10.6^{+3.7}_{-3.9}$	$3.1^{+0.9}_{-1.4}$	$10.94^{+1.62}_{-1.26}$	$8.92^{+5.08}_{-8.91}$
Halo	462	0	$241.81^{+80.89}_{-36.89}$	$-0.87^{+0.32}_{-0.63}$	$0.27^{+0.13}_{-0.27}$	259^{+300}_{-493}	$24.5^{+5.6}_{-3.3}$	$3.6^{+1.6}_{-1.6}$	NA	$10.14^{+3.86}_{-8.12}$
Sirus	10,036	8	$21.24^{+10.74}_{-8.61}$	$-0.05^{+0.18}_{-0.21}$	$0.01^{+0.12}_{-0.03}$	1925^{+25}_{-25}	$4.0^{+0.7}_{-0.6}$	$1.3^{+1.1}_{-1.2}$	NA	$1.65^{+2.68}_{-1.65}$
Hercules	8,170	8	$72.09^{+15.10}_{-14.95}$	$-0.03^{+0.24}_{-0.29}$	$0.03^{+0.16}_{-0.06}$	1510^{+76}_{-54}	$7.8^{+1.9}_{-1.6}$	$1.5^{+1.0}_{-1.0}$	NA	$2.05^{+3.19}_{-2.05}$
Pleiades/Hyades	5,668	4	$44.69^{+7.30}_{-6.40}$	$0.00^{+0.21}_{-0.27}$	$0.01^{+0.13}_{-0.05}$	1573^{+88}_{-32}	$4.5^{+0.6}_{0.7}$	$1.5^{+0.9}_{-1.2}$	NA	$2.06^{+2.86}_{-2.06}$
Coma	1,823	2	$20.00^{+9.30}_{-3.58}$	$0.03^{+0.18}_{-0.25}$	$0.01^{+0.12}_{-0.02}$	1800^{+50}_{-41}	$1.90^{+0.6}_{-0.7}$	$1.0^{+1.3}_{-1.2}$	NA	$1.62^{+2.56}_{-1.62}$
γLeo	1,202	0	$49.10^{+18.55}_{-11.79}$	$-0.10^{+0.21}_{-0.25}$	$0.04^{+0.12}_{-0.04}$	1929^{+39}_{-57}	$6.7^{+1.8}_{-0.9}$	$1.8^{+1.0}_{-1.3}$	NA	$3.57^{+5.05}_{-3.57}$
Arcturus	523	2	$101.18^{+28.60}_{-6.59}$	$-0.33^{+0.37}_{-0.33}$	$0.23^{+0.14}_{-0.23}$	1137^{+19}_{-37}	$11.5^{+1.5}_{-0.8}$	$2.2^{+1.5}_{-1.1}$	NA	$5.39^{+8.61}_{-5.39}$
HR1614	469	1	$71.64^{+7.87}_{-5.52}$	$-0.08^{+0.30}_{-0.37}$	$0.09^{+0.21}_{-0.09}$	1355^{+26}_{-36}	$8.1^{+0.8}_{-0.6}$	$2.0^{+1.0}_{-1.1}$	NA	$4.17^{+6.68}_{-4.17}$
A1/A2	432	0	$51.15^{+15.22}_{-10.09}$	$-0.27^{+0.24}_{-0.22}$	$0.06^{+0.12}_{-0.06}$	2186^{+22}_{-35}	$10.8^{+1.2}_{-0.5}$	$2.0^{+0.9}_{-1.1}$	NA	$3.84^{+5.18}_{-3.17}$
Wolf630	273	3	$35.43^{+8.42}_{-3.34}$	$-0.02^{+0.21}_{-0.26}$	$0.04^{+0.11}_{-0.04}$	1709^{+20}_{-32}	$2.9^{+0.4}_{0.2}$	$1.5^{+1.1}_{-1.1}$	NA	$2.51^{+6.50}_{-2.51}$
Dehnen	118	0	$52.67^{+7.66}_{-3.36}$	$-0.09^{+0.24}_{-0.28}$	$0.05^{+0.12}_{-0.05}$	1688^{+21}_{-30}	$5.5^{+0.4}_{-0.3}$	$1.8^{+1.2}_{-1.1}$	NA	$3.83^{+6.11}_{-3.83}$
Antoja12	128	0	$98.26^{+7.62}_{-13.87}$	$-0.14^{+0.22}_{-0.21}$	$0.08^{+0.19}_{-0.08}$	1495^{+243}_{-39}	$9.7^{+1.9}_{-1.3}$	$1.9^{+1.0}_{-1.0}$	NA	$3.50^{+5.36}_{-3.50}$
ϵInd	61	0	$111.38^{+12.31}_{-6.02}$	$-0.33^{+0.33}_{-0.30}$	$0.25^{+0.09}_{-0.25}$	1268^{+22}_{-37}	$12.5^{+0.5}_{-1.0}$	$2.3^{+1.4}_{-0.8}$	NA	$6.00^{+8.00}_{-6.00}$

Note—Units are the same as Table 3.

B. MCMC RESULTS FROM *THE JOKER*

For systems with a unique orbital solution returned by the rejection sampling from *The Joker*, we first generated 80,000,000 prior samples to mitigate sampling incompleteness. If a unique solution was still obtained after this extensive sampling, the resulting posterior samples from The Joker were used to initialize a standard MCMC process to further refine the posterior distributions of the orbital parameters (i.e., P, e, ω, M_0, K, and v_0). The MCMC sampling was performed using the PyMC3 package (Abril-Pla et al. 2023), with 5,000 draws and 20 chains. The 1σ uncertainties were defined by the 15.9th and 84.1st percentiles of the marginalized posterior distributions. As an illustrative example, Figure B1 shows the corner plot for TIC 168704855, which demonstrates good convergence. In some cases, the MCMC chains may exhibit poor convergence. To ensure reliability, we recommend utilizing posterior distribution results only when the Gelman-Rubin statistic is less than 1.1 (Gelman & Rubin 1992), indicating well-converged chains.

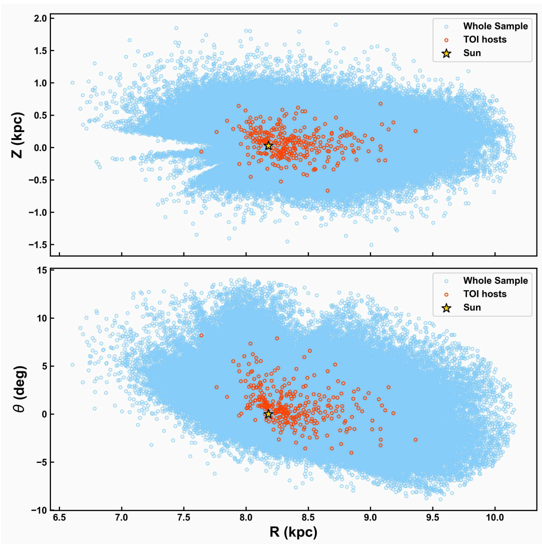

Figure A1. Same as Figure 2 for the LRS sample.

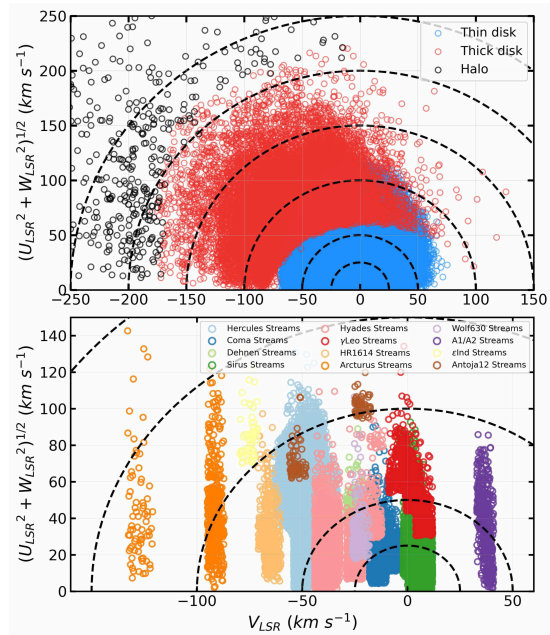

Figure A2. Same as Figure 3 for the LRS sample.

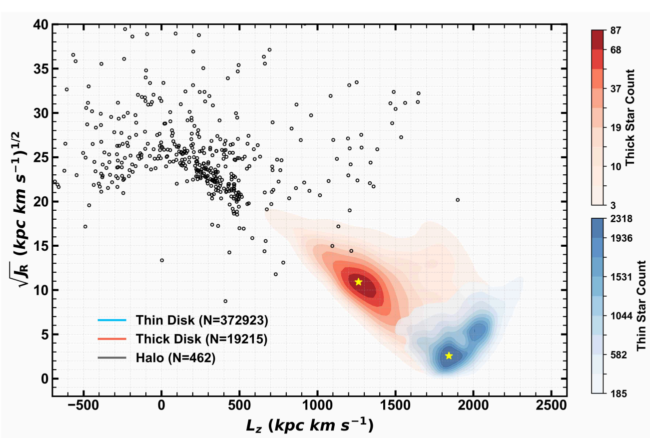

Figure A3. Same as Figure 4 for the LRS sample.

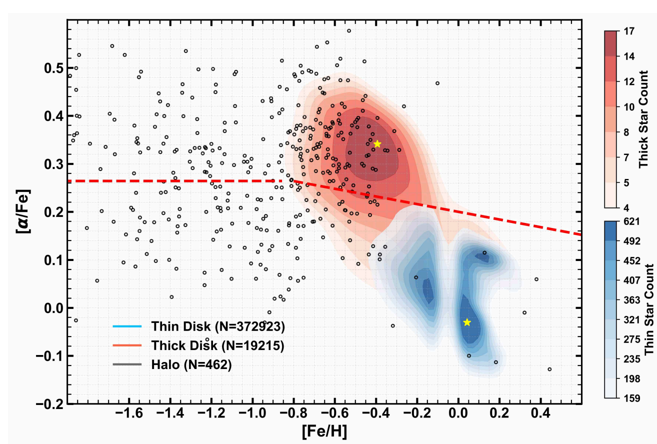

Figure A4. Same as Figure 5 for the LRS sample.

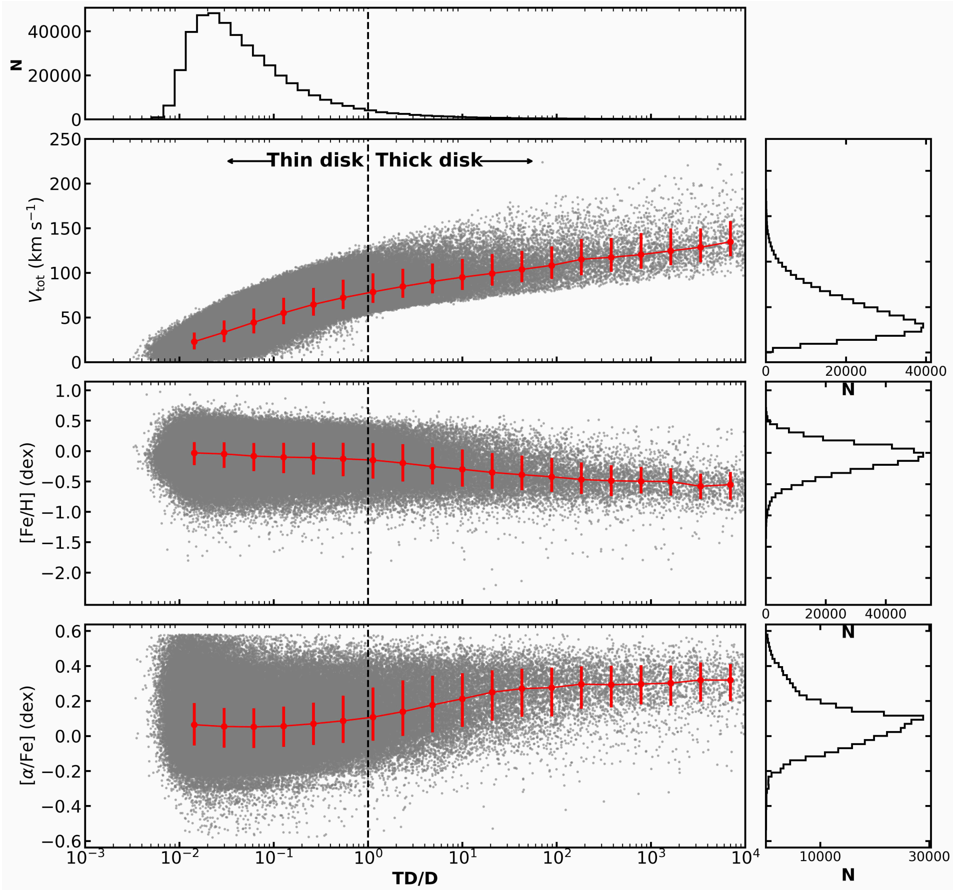

Figure A5. Same as Figure 6 for the LRS sample.

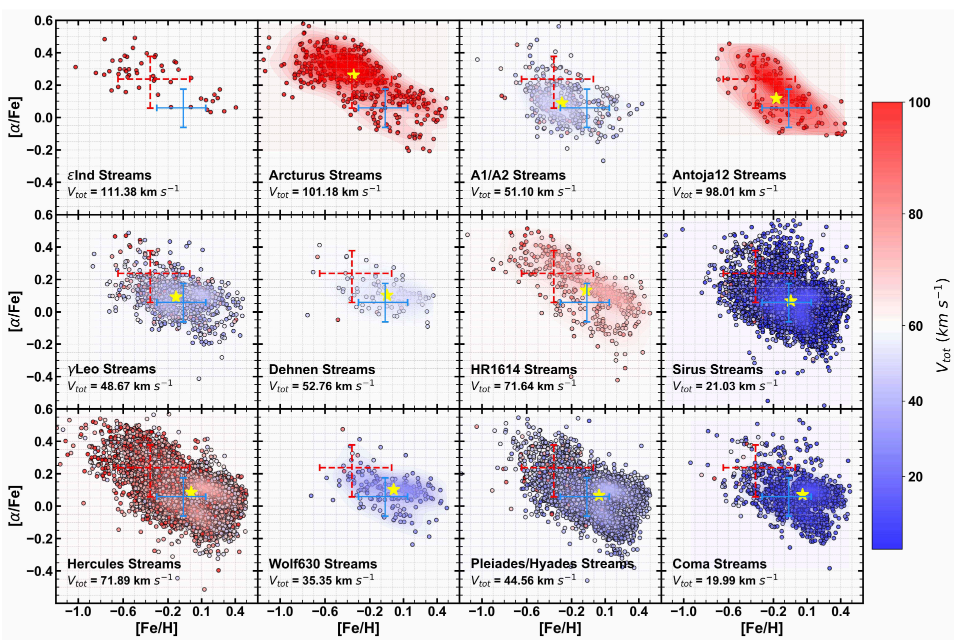

Figure A6. Same as Figure 7 for the LRS sample.

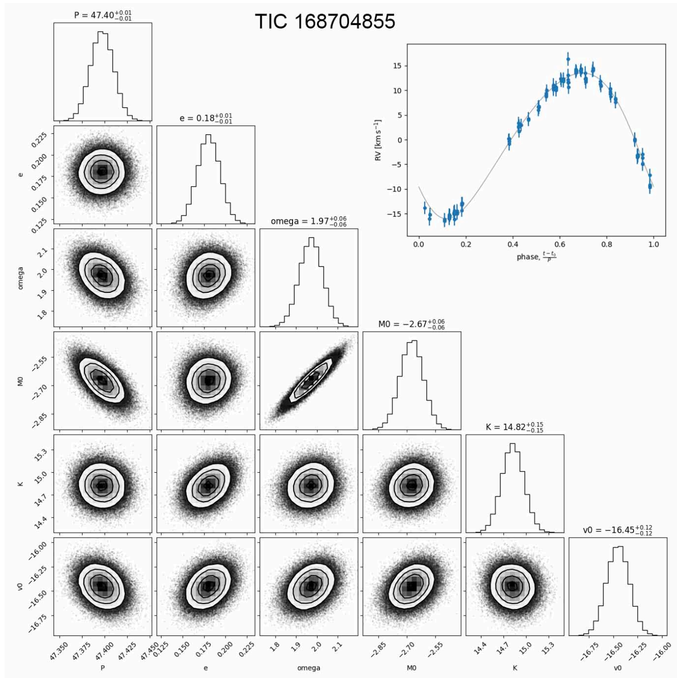

Figure B1. Corner plot for TIC 168704855 on the bottom left showing the posterior distributions of orbital parameters. The phase-folded RV curve and the corresponding fitting result are displayed in the top right panel.